

UKAEA-CCFE-PR(23)137

Renato Pero, Nicholas Randall, Damian Frey, Remo  
Widmer, Tim Darby, Lee Aucott, Chris Hardie, Sunil  
Pak, Philippe Maquet, Andrew Bushby

**New stress-strain indentation  
mapping methodology for measuring  
mechanical properties across  
diffusion-bonded interface of  
International Thermonuclear  
Experimental Reactor (ITER) window  
assembly**

Enquiries about copyright and reproduction should in the first instance be addressed to the UKAEA Publications Officer, Culham Science Centre, Building K1/O/83 Abingdon, Oxfordshire, OX14 3DB, UK. The United Kingdom Atomic Energy Authority is the copyright holder.

The contents of this document and all other UKAEA Preprints, Reports and Conference Papers are available to view online free at [scientific-publications.ukaea.uk/](https://scientific-publications.ukaea.uk/)

# **New stress-strain indentation mapping methodology for measuring mechanical properties across diffusion-bonded interface of International Thermonuclear Experimental Reactor (ITER) window assembly**

Renato Pero, Nicholas Randall, Damian Frey, Remo Widmer, Tim Darby, Lee Aucott, Chris Hardie, Sunil Pak, Philippe Maquet, Andrew Bushby



# New stress-strain indentation mapping methodology for measuring mechanical properties across diffusion-bonded interface of International Thermonuclear Experimental Reactor (ITER) window assembly

**Authors:** Renato Pero<sup>1</sup>, Nicholas Randall<sup>1</sup>, Damian Frey<sup>1</sup>, Remo Widmer<sup>1</sup>, Tim Darby<sup>2</sup>, Lee Aucott<sup>2</sup>, Chris Hardie<sup>2</sup>, Sunil Pak<sup>3</sup>, Philippe Maquet<sup>4</sup>, and Andrew Bushby<sup>5</sup>

<sup>1</sup> Alemnis AG, Business Park Gwatt, Schorenstrasse 39, 3645 Gwatt (Thun), Switzerland

<sup>2</sup> United Kingdom Atomic Energy Authority (UKAEA), Culham Science Centre, Abingdon, OX14 3DB, UK

<sup>3</sup> International Thermonuclear Experimental Reactor (ITER) Organization, Route de Vinon-sur-Verdon, St. Paul Lez Durance, 13067, France

<sup>4</sup> Bertin Technologies, 155 Rue Louis Armand, Aix en Provence, 13290, France

<sup>5</sup> Queen Mary University, Mile End Rd, Bethnal Green, London E1 4NS, UK

**Proposed journal:** Journal of Nuclear Materials

## Abstract

The International Thermonuclear Experimental Reactor (ITER) is an international nuclear fusion research and engineering project with the aim to prove the feasibility of nuclear fusion as a large-scale carbon-free source of energy. The reactor vessel contains several diagnostic windows that provide a line of sight to the plasma. Design and qualification of such windows is challenging due to severe in-service conditions and the necessity to combine glasses with metals. One specific window is composed of fused silica glass that is connected to an Inconel ferrule via an aluminium bonding layer, where the joint is consolidated through a diffusion bonding process. The precise design parameters of this window are subject to continuous improvements. A major role in this effort plays three-dimensional finite element model (FEM). Importantly, these FEM simulations require stress-strain curves as input parameters. Such curves are difficult to obtain, especially from complex systems with dissimilar joints. In the present paper a novel methodology based on dynamic spherical nanoindentation has been developed and applied to map the stress-strain characteristics across the diffusion bonded joints. The methodology takes inspiration from the well-known theory to extract stress-strain curves from spherical nanoindentation which has been applied to automated large indentation map and relies on a fully automated post-processing protocol to extract tensile-like properties (*i.e.*, yield stress, yield strain, work hardening parameter and elastic modulus). Results show outstanding correlation with microstructural changes across the bonded cross-section, including grain refinement and twinning at the Inconel/aluminium interface.

## 1 Introduction

The International Thermonuclear Experimental Reactor (ITER) is an international project, with 35 nations collaborating to design, construct and operate a prototype controlled nuclear fusion reactor in southern France (Figure 1). The ultimate goal of the ITER is to produce 500 MW of fusion power with a ten-fold return on input energy (*i.e.*, to produce 500 MW with a 50 MW input power). To achieve this goal, a mixture of deuterium and tritium will be required in the vessel. As a result, the ITER site is considered to be a basic nuclear installation (INB No 174) as defined in French law [1] and as such is regulated by the French Nuclear Safety Authority (ASN).

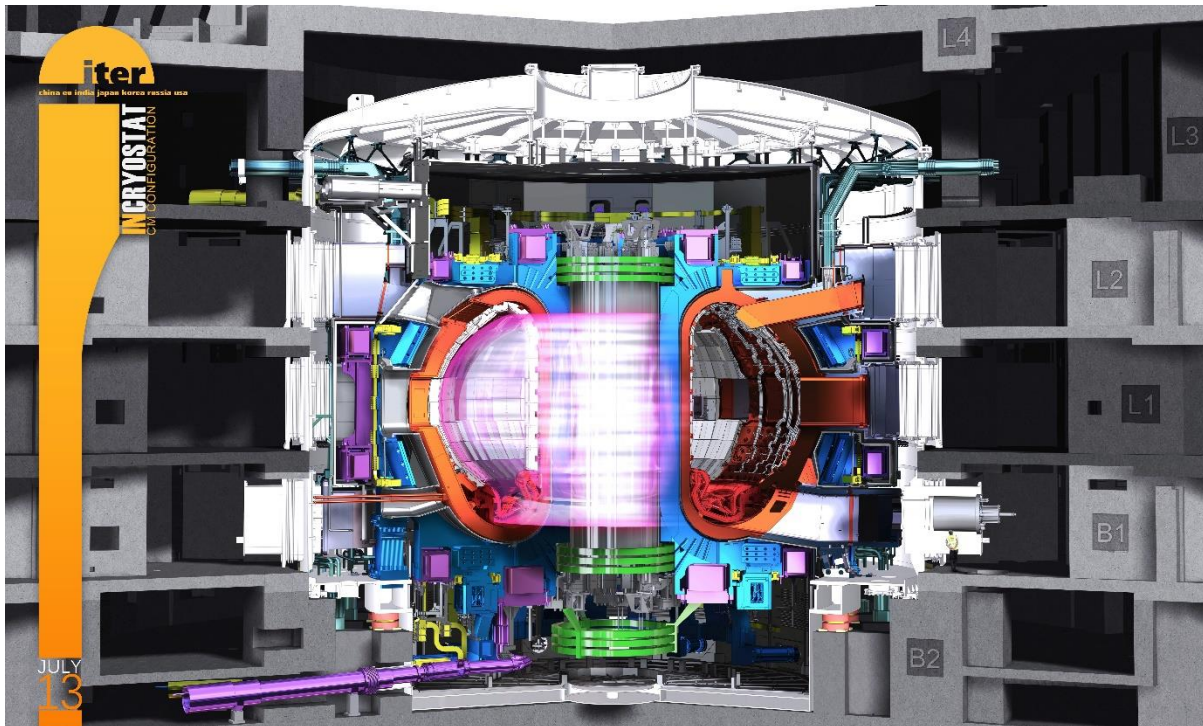


Figure 1: CAD model of the ITER tokamak reactor.

As the reactor contains several diagnostic systems which require line of sight at various wavelengths to the plasma, it is necessary to include windows into the first containment structure [2]. The current catalogue of standard diagnostic window assemblies offers nine configurations of fused silica windows in various sizes with nominal clear view diameters varying from 25 mm to 160 mm, an example can be seen in Figure 2a [3]. A CAD model of a typical ITER diagnostic window assembly is illustrated in Figure 2b. Figure 2c presents a CAD model of the key components and material configuration concerned in the diffusion bonding process. An aluminium interlayer is used to bond a tapered fused silica optic into the matched taper of an Inconel 625 ferrule (Figure 2c). Prior to the process, the aluminium is cleaned to remove contaminants. A bonding furnace is used to apply a large load and heat the assembly up to 50-60% of the melting temperature to press the aluminium into the joint. Specific details concerning the process parameters is commercially sensitive, therefore only an overview of the process will be discussed in this paper [3].

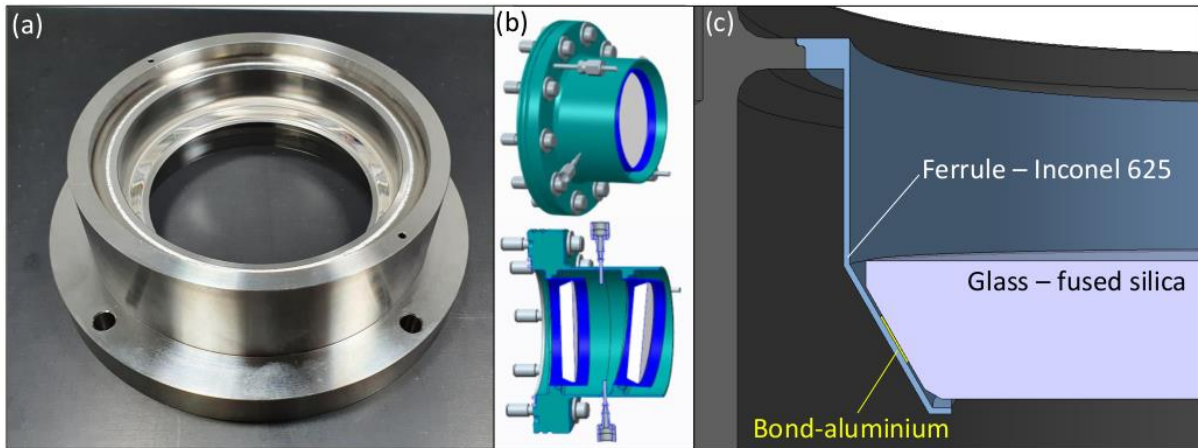


Figure 2: (a) photograph of the finished diffusion bonded window assembly, (b) CAD model of the ITER diagnostic window assemblies and (c) CAD model illustrating key components associated with the diffusion bonding process.

Prior investigations made by some of the authors [3] on analogous diffusion bonded joints underlined two critical points. Firstly, fused silica is believed to accumulate considerable residual stress during manufacturing that has a detrimental effect on lifetime of the assembled component and which at the current state of the art cannot be reliably measured [3]. Secondly, the development of a procedure for the qualification of key components composed of ceramic/metal bonded joints is challenging and the object of continuous effort for improvement [3]. The procedure involves the use of three-dimensional finite element modeling (FEM) [3], which requires stress-strain curves as input.

Measuring a stress-strain curve is one of the most widespread methods to quantify mechanical behaviour of materials. However, the accurate extraction of spatially resolved stress-strain curves in complex systems characterised by local gradients of mechanical properties (for example due to bonded joints, composite materials, thin films, and additively manufactured components) can be challenging to near-impossible on the macro-scale. On the micro-scale, on the other hand, spherical nanoindentation has proven to be a relatively simple yet effective testing methodology to extract stress-strain behaviour of materials, as supported by a number of publications [4] [5] [6] [7] [8] [9] [10] [11] [12].

One of the advantages of spherical nanoindentation is that it can probe the elastic-plastic transition during the test and thus provide a yield point for the specified contact conditions. However, the traditional approach of making a progressive load multicycle with sufficient cycles to extrapolate yield point is very time-consuming as each cycle must be unloaded before the next [10] [11] [12] and data postprocessing for yield point identification has never been fully automated. This study introduces the concept of dynamic spherical nanoindentation which can provide the same data in a fraction of the time and, when combined with fast mapping, allows the yield point to be mapped in an efficient and automated manner.

Previous work [13] has shown the advantage of large arrays of indentations (sometimes referred to as grid indentation) where the resulting data is analysed as a batch and statistical analysis can yield average values of mechanical properties, as well as surface fractions and 2D mechanical property maps [14]. However, such large mapping techniques have never previously been combined with dynamic spherical nanoindentation. The extraction of the yield stress values from progressive-load multicycle spherical indentations in combination with mapping indentation has already been

proposed by one of the authors [6], though a non-automated postprocessing was used. The present paper has been inspired by this pioneering study [6] and aims to employ the more efficient dynamic spherical nanoindentation method combined with automated maps combined with more advanced data batch processing protocol for automated extraction of yield stress, yield strain, work hardening parameters, elastic modulus, and hardness, without user intervention.

The present paper aims to help in relaxing the criticisms raised in [3] offering an innovative testing method that, on the one hand, helps in the qualification of dissimilar bonded joints and, on the other hand, provides local tensile-like mechanical properties. The methodology combines the well-known and robust theory to extract tensile-like stress-strain curves from dynamic spherical indentations [4] [5] [6] [7] [8] [9] [10] [11] [12] and automated large indentation mapping [13] [14]. Diffusion-bonded Inconel–aluminium–fused silica samples have been selected as target candidates to test and validate the present methodology not only for their practical relevance in the nuclear engineering field [3], but also for the presence of fused silica in the joint, which is a common reference material for nanoindentation. It thus also offers a unique opportunity to validate results of the present methodology. As FEM simulations mainly focus on the prediction of the behaviour of the aluminium bond, the present methodology has been optimized for indentation of aluminium [3]. The paper includes the description of a tip area calibration (TAC) procedure to account for non-ideal indenter tip shape based on indentation on 4 reference materials. Moreover, an in-depth quantification of artifacts that can generally affect indentation results has been carried out, namely, the influence of different indenter tip shapes (or tip shape effect), the spacing between indentations in a map, the indentation size effect (ISE), and the strain rate sensitivity. Finally, a systematic investigation on the difference between dynamic and quasistatic indentations revealed that hardness of elastoplastic materials is often underestimated by dynamic indentation, and that the discrepancy is larger in highly strain rate sensitive materials [15]. This suggests that any dynamic indentation analysis should be completed by a complementary investigation on the strain rate sensitivity of the target materials.

## **2 Materials and Method**

Two diagnostic windows from the ITER (see Figure 2) have been sliced, first with a high-pressure water cutter and then with a slow-speed saw, to obtain 6 cross-sectioned samples (Samples A to F) with a thickness of approximately 1.25 mm. Each cross-section exhibits a full length of the Inconel/aluminium/fused silica bonded joint (Figure 2c). Notice that most of the fused silica has been removed before cutting to simplify slicing procedure. In order to perform metallographic and nano-indentation analysis, each slice has been mounted on a standard 12.5 mm SEM stub using Crystal Bond adhesive. The exposed cross-sections were then polished using SiC abrasive papers with a grit size from P80 to P1200. The mirror-finishing step was initiated with 3 and 1  $\mu\text{m}$  diamond suspensions on a Trident pad with 25 N applied force per sample at 300 rpm for 180 s for each suspension size. Then final polish has been performed with a diamond suspension on a Chemo pad with 25 N applied force per sample at 150 rpm for 180 s. Samples have been ultrasonically cleaned in isopropanol after each polishing stage.

## **3 Indentation test procedure**

The nanoindentation testing has been performed with an Alemnis Standard Assembly (ASA) combined with an Enhanced Controller (ECO) (Alemnis AG, Thun, Switzerland). The indenter is equipped with a standard load cell having a maximum load and RMS noise of 2.5 N and 15  $\mu\text{N}$  respectively, and a 40  $\mu\text{m}$  piezo stack actuator. The frame compliance was as low as 4.10  $\mu\text{m}/\text{N}$ . Tests has been carried out *in-situ* in a Zeiss DSM962 Scanning Electron Microscope (SEM, Carl Zeiss Digital Innovation GmbH, Dresden Germany). Two spherical diamond indentation tips manufactured by Synton-MDP AG (Nidau, Switzerland) have been selected for the testing campaign, having cone angle of  $90^\circ$  and nominal radius of 2.05 and 4.92  $\mu\text{m}$ , for clarity they will be hereinafter named as 2 and 5  $\mu\text{m}$  tips, respectively. For comparison purpose, also a diamond Berkovich tip has been employed.

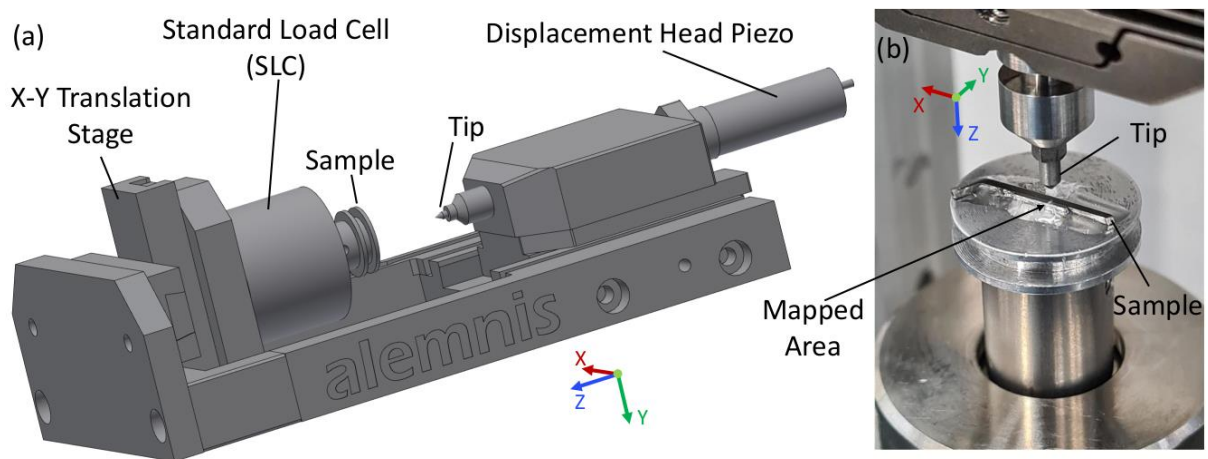


Figure 3: (a) CAD model of the Alemnis Standard Assembly (ASA) set-up used for the present testing campaign, and (b) photo of a sample mounted on the ASA.

The first step of the investigation consisted of the determination of the tip area function of the selected tips via a dedicated analysis performed on 4 different reference materials, namely, fused silica, Silicon "Si(100)", gallium arsenide "GaAs(100)" and sapphire. Details on the procedure are given in Appendix A.

The indentation protocol has been designed in true-displacement control and consists of 4 main segments, namely, fast-approaching, initial loading, loading in continuous stiffness measurement (CSM) mode and unloading. The identification of a single experimental protocol suitable to test three very different materials (*i.e.*, Inconel, aluminium and fused silica) has been achieved via trial-and-error and the "mixed-mode" protocol interface built-in in the Alemnis software. In the present study *mixed-mode* has been employed to combine true-displacement control mode with load targets that define the end of each indentation segment. The *mixed-mode* capability significantly expands the range of possible protocols that can be defined to test systems composed of materials or phases with very different mechanical properties.

For the 5  $\mu\text{m}$  tip, the fast-approaching segment with a target load of 500  $\mu\text{N}$  at a displacement rate of 0.8  $\mu\text{m}/\text{s}$  is followed by an initial loading segment with a lower displacement rate of 100  $\text{nm}/\text{s}$  until a load target of 2.5  $\text{mN}$ . Keeping the displacement rate constant for 1200  $\text{nm}$ , a harmonic oscillation

having 10 Hz frequency and 10 nm amplitude is superimposed to the loading curve defining the CSM segment. Notice that the maximum depth of this protocol is defined by the combination of the displacement reached at 2.5 mN and the 1200 nm of the CSM segment. Finally, a displacement rate of 50 nm/s has been imposed for the retraction segment.

Preliminary tests showed that the 5  $\mu\text{m}$  tip gave the most satisfactory results and it was therefore selected to carry out most of the quantitative indentation mapping analysis. A second set of analyses limited to a smaller number of indentations has been performed using the 2  $\mu\text{m}$  tip according to the following protocol. The fast-approaching segment with a target load of 100  $\mu\text{N}$  at a displacement rate of 0.8  $\mu\text{m/s}$  is followed by an initial loading segment with a lower displacement rate of 100 nm/s until a load target of 500  $\mu\text{N}$ . Keeping the displacement rate constant for 400 nm, a harmonic oscillation having 10 Hz frequency and 6 nm amplitude is superimposed to the loading curve defining the CSM segment. Notice that the maximum depth of this protocol is defined by the combination of the displacement reached at 0.5 mN and the 400 nm of the CSM segment. Finally, a displacement rate of 50 nm/s has been imposed for the retracting segment.

During preliminary tests it was established that the use of the 2  $\mu\text{m}$  tip and its respective indentation protocol gives good results when applied to aluminium and Inconel. However, the same protocol was not suitable to adequately test fused silica. These results have therefore been discarded. The ideal parameters to adequately analyse fused silica can be found by increasing the oscillation frequency or decrease the displacement rate, however this then has an adverse impact on the mechanical response of aluminium as it has been found to be markedly strain rate dependent (see Appendix E) [15]. As the validation of the mechanical behaviour of aluminium for FEM simulations is considered a priority objective of the present study [3], it has been decided not to change the displacement rate and oscillation frequency; at the expense of quality of the results on fused silica. Note that typical indentation results such as hardness and elastic modulus from fused silica survey are still included in the present analysis and help in the validation of the current experimental procedure.

Indentation map protocols have been defined to characterise the mechanical properties of samples across the 3 materials including the two interface regions that compose the diffusion bonded joints. Four samples (Samples A–D) were mapped using the 5  $\mu\text{m}$  tip, with a minimum of 1350 indentations per map. The indentations were equally spaced by 10  $\mu\text{m}$  in both x and y, covering an overall surface of approximately 200  $\mu\text{m}$  x 650  $\mu\text{m}$ . The x-axis of each map has been roughly aligned with the Inconel/aluminium interface. A number of indentation maps with a minimum number of 300 indentations per map have been performed using the 2  $\mu\text{m}$  tip on Sample B, E and F. This allowed validation of the results obtained with the 5  $\mu\text{m}$  tip, and investigation of the effect of different mapping parameters, such as spacing (between 5 and 10  $\mu\text{m}$  in x and y) and mapping path, which are discussed in detail in the Appendices B and C, respectively. An additional map on Sample B using a diamond Berkovich tip aimed at studying strain rate sensitivity and indentation size effects (ISE).

Post processing of indentation curves has been done with the dedicated software *Alemnis Materials Mechanics Data Analyser for Indentation Stress Strain* (AMMDA ISS). The software automatically applies an unloading analysis according to the ISO 14577 protocol [16] and a stress-strain analysis as described in the next section (*Theory and Calculations*). As different post processing parameters might be demanded by each specific phase (for instance, the Poisson's ratio [16] for the unloading analysis considerably changes from aluminium to fused silica), AMMDA ISS allows the assigning of different analysis parameters and models to curves of different materials. To identify in advance the curves of different materials, filters based on the x and y coordinates of indentations or on the maximum load/displacement can be applied. In this study, indentation curves have been divided in 5 groups, namely, Inconel base, aluminium base, fused silica base, Inconel/aluminium (INCO/Al) interface and

aluminium/fused silica (Al/FS) interface. Metallography by means of SEM has been performed using either the Zeiss DSM962 or a TESCAN MIRA3 (TESCAN ORSAY HOLDING, a.s., Brno, Czech Republic) SEMs.

#### 4 Theory and Calculations

The reference stress ( $\sigma$ ) is given by the following relationship originally proposed by Tabor [17] [4]:

$$\sigma(h_c) = \frac{H(h_c)}{K} \quad \text{Eq. 1}$$

where  $H(h_c)$  is the indentation hardness as a function of contact depth ( $h_c$ ) and  $K$  is the indentation stress constraint factor that is a constant close to 3 [17] [11]. The  $H - h_c$  relationship has been measured using dynamic spherical indentation test, also known as continuous stiffness measurement (CSM) indentation test [18], but other methodologies, e.g., progressive load multicycle [6] [7], can be applied as well. The CSM indentation is a dynamic mechanical testing methodology that consists of the superimposition of a harmonic oscillation on the loading curve of an indentation [18] [19]. The main advantage of the CSM methodology is that the contact stiffness (given as the ratio of the load amplitude to the displacement amplitude for elastic contact), load, and displacement can be measured for each individual unloading segment of each cycle, allowing to build both elastic modulus and hardness depth profiles [18] [8] [9].

The reference strain ( $\varepsilon$ ) is given by the following relationship [8]:

$$\varepsilon(h_c) = C \frac{a(h_c)}{R(h_c)} \quad \text{Eq. 2}$$

where  $C$  is a constant close to 0.2 [8],  $R$  is the indenter radius and  $a$  is the radius of the spherical imprint. Notice that the radius of an ideal indenter ( $R_i$ ) is constant with the contact depth and the relationship between contact depth and radius of the ideal spherical imprint can be obtained by geometrical consideration as [5] [8] [4] [6]:

$$a(h_c) = \sqrt{2 R_i h_c - h_c^2} \quad \text{Eq. 3}$$

In present study, two indentation tips with 2.05  $\mu\text{m}$  and 4.92  $\mu\text{m}$  ideal radii have been employed (for simplicity named 2  $\mu\text{m}$  and 5  $\mu\text{m}$ ). Their ideal  $\varepsilon - h_c$  relationship is shown in Figure 4.

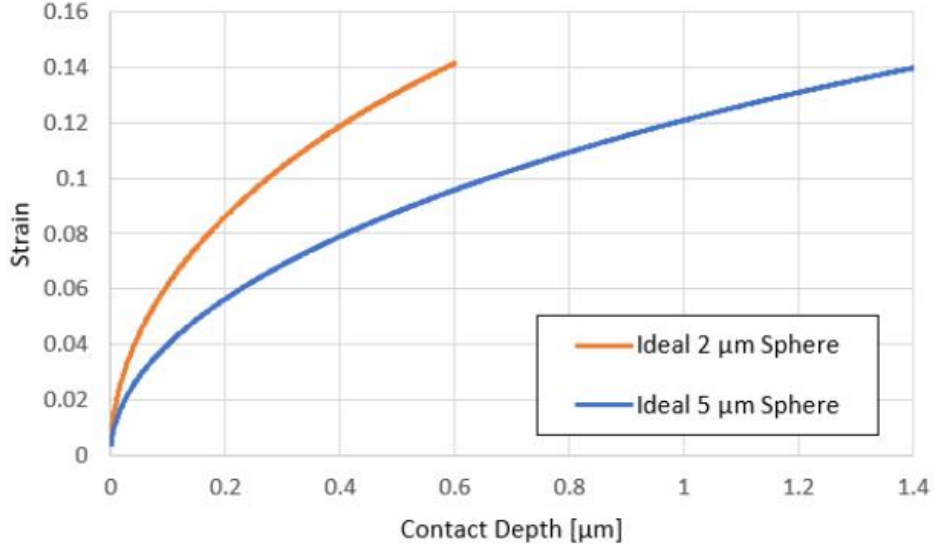


Figure 4: Strain vs Contact Depth for 2 μm and 5 μm ideal spherical tips using Equation 2.

The spherical indenter in use is composed of a spherical end supported by a truncated-conical section. With increasing depth, the geometry of the indenter progressively changes from a spherical to conical. The theoretical depth ( $h_{th}$ ) at which this spherical-to-conical transition occurs is defined by the tip radius and the cone angle ( $\alpha$ ) as following:

$$h_{th} = R_i \left( 1 - \sin\left(\frac{\alpha}{2}\right) \right) \quad \text{Eq. 4}$$

The ideal  $\varepsilon - h_c$  relationships in Figure 4 are therefore interrupted at a maximum contact depth of 600 nm and 1.4 μm, respectively, which are the theoretical depths of spherical-to-conical transition for the 2 μm and 5 μm radius, respectively, having a 90° conical angle. For a real indenter, both the effective radius ( $R_{eff}$ ) and its related effective radius of the spherical imprint ( $a_{eff}$ ) can be estimated from the calibrated tip area function ( $A_p(h_c)$ ) as follows [5] [6]:

$$R_{eff}(h_c) = \frac{a_{eff}^2 + h_c^2}{2 h_c} \quad \text{Eq. 5}$$

$$a_{eff}(h_c) = \sqrt{\frac{A_p(h_c)}{\pi - h_c^2}} \quad \text{Eq. 6}$$

Details on the estimation of  $A_p$  are given in Appendix A.

Typical load-displacement and  $\sigma - \varepsilon$  curves of fused silica, Inconel, and aluminium obtained with a 5 μm spherical indenter, are shown in Figure 5. The fused silica curve exhibits a well-defined linear elastic behaviour at relatively small strain. The slope of the stress-strain curve suddenly drops with increasing strain. This abrupt change in slope identifies the yielding point of the material.

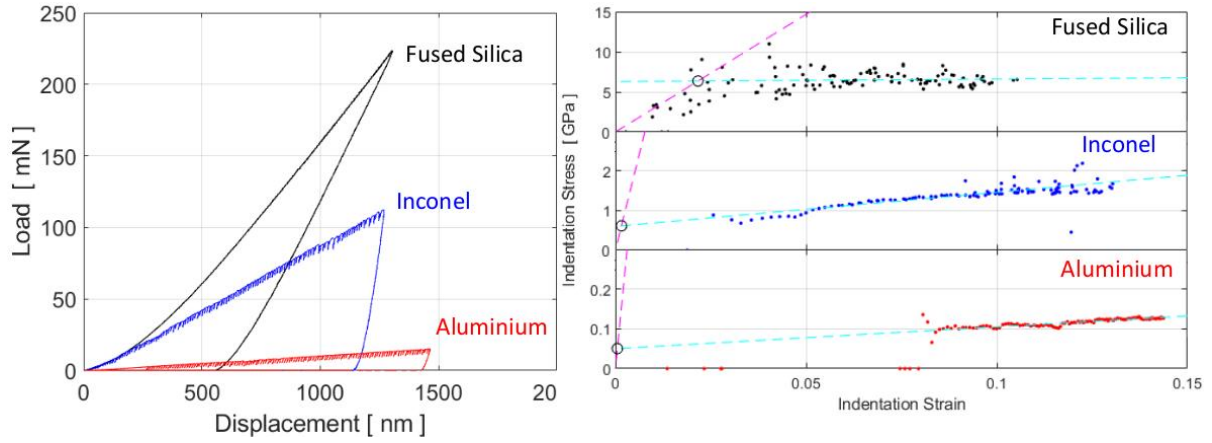


Figure 5: Typical (a) Load-Displacement curves and (b) Stress-Strain curves for fused silica, Inconel and aluminium obtained by 5  $\mu\text{m}$  spherical indentation. Dashed purple lines in (b) have been calculated from Eq. 9 to model the linear elastic portion of the stress-strain curve. Dashed light blue lines in (b) are linear fittings of the elastoplastic hardening.

The application of the current theory to large indentation maps raises the need of identification of yield point via an automated post-processing protocol. To implement such an automated protocol, the Hertz theory on contact between sphere and elastic half space has been invoked [20] which defines the radius of the elastic contact between a sphere and a plane ( $a_{el}$ ) as

$$a_{el} = \left( \frac{3 P(h_C) \cdot R_{eff}(h_C)}{4 E_*} \right)^{\frac{1}{3}} \quad \text{Eq. 7}$$

where  $P$  is the indentation load and  $E_*$  is the reduced modulus of the contact given by the following relationship [5] [16] [8] [4] [20]:

$$\frac{1}{E_*} = \left( \frac{1 - \nu_i^2}{E_i} + \frac{1 - \nu_s^2}{E_s} \right) \quad \text{Eq. 8}$$

where  $E_i$  and  $E_s$  are elastic modulus of indenter and sample, respectively, and  $\nu_i$  and  $\nu_s$  are Poisson's ratio of indenter and sample, respectively [16]. Notice that  $E_s$  can be measured from each individual indentation test according to the ISO14577 [16].

The Elastic Stress ( $\sigma_{el}$ ) is then defined as [20] [21]:

$$\sigma_{el} = \frac{3 P(h_C)}{2 \pi a_{el}^2} \approx 0.4 \left( \frac{P(h_C) \cdot E_*^2}{R_{eff}^2(h_C)} \right)^{\frac{1}{3}} \quad \text{Eq. 9}$$

As the Hertz theory is shown to model very well the elastic behaviour of fused silica (this will be addressed in the *Discussion* section), it has been chosen in the present study to characterize the elastic behaviour in the stress-strain curves. Inconel and aluminium exhibit marked plasticity at the early stages of indentation (see in Figure 5b), even before the first oscillation cycle of a CSM indentation. This implies that depending on the indenter size it is often not possible to observe their elastic behaviour using spherical CSM indentation. The Hertz model [20] offers a convenient methodology to overcome this limitation.

Finally, linear fitting has been performed on the elastoplastic section of the stress-strain curve, as this is often a good approximation for material hardening [4] [6]. The slope of the linear fit is defined here as the work hardening parameters expressed in [GPa].

## 5 Results

A top view backscattered electron (BSE) SEM image of Sample B after 5  $\mu\text{m}$  indentation mapping is shown in Figure 6a, where the mapped area is indicated by the dashed rectangle. The mapping has been performed sufficiently far away from any defects (*e.g.*, cracks in fused silica) or edges of the sample. Notice that each line of the indentation map has been performed along the x axis of the indenter translation stage which has been selected to be parallel to the INCO/Al interface. A secondary electron (SE) SEM image of Sample A while mounted on the Alemnis ASA is shown in Figure 6b. In order to simultaneously observe the sample surface and the 5  $\mu\text{m}$  indenter tip, the ASA is tilted such that its z translation axis is oriented 80° with respect to the electron beam. Notice that the INCO/Al interface here is aligned with the x axis of the ASA translation stage (Figure 6b), *i.e.* rotated by 90° in the x-y plane with respect to Sample B in Figure 6a. The orientation selected in Figure 6b offers a clear view of the two interfaces.

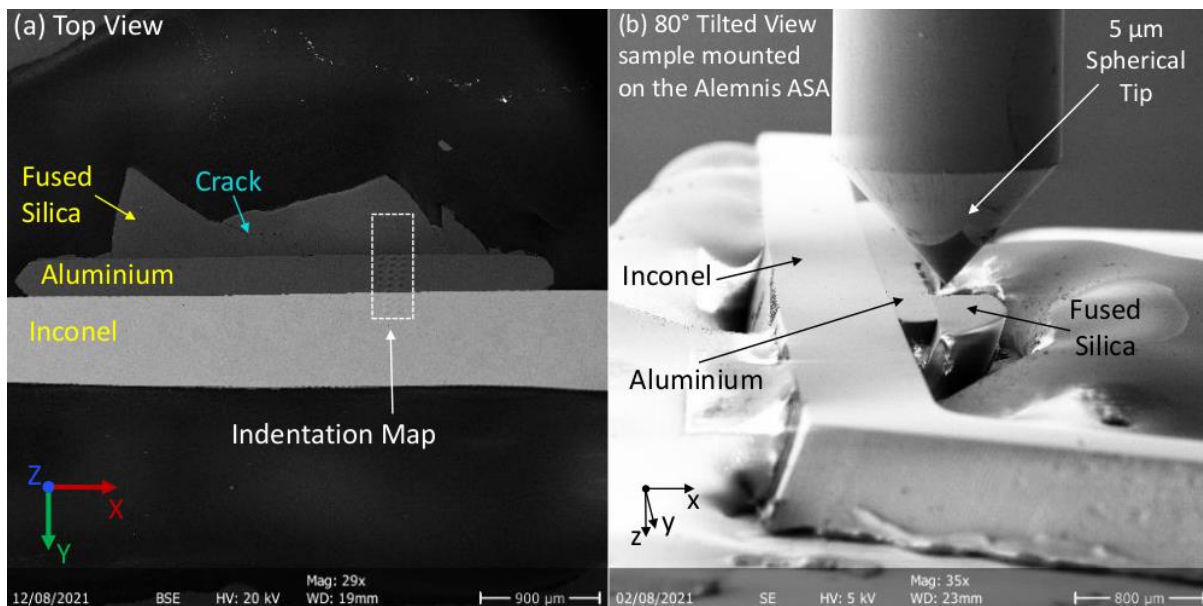
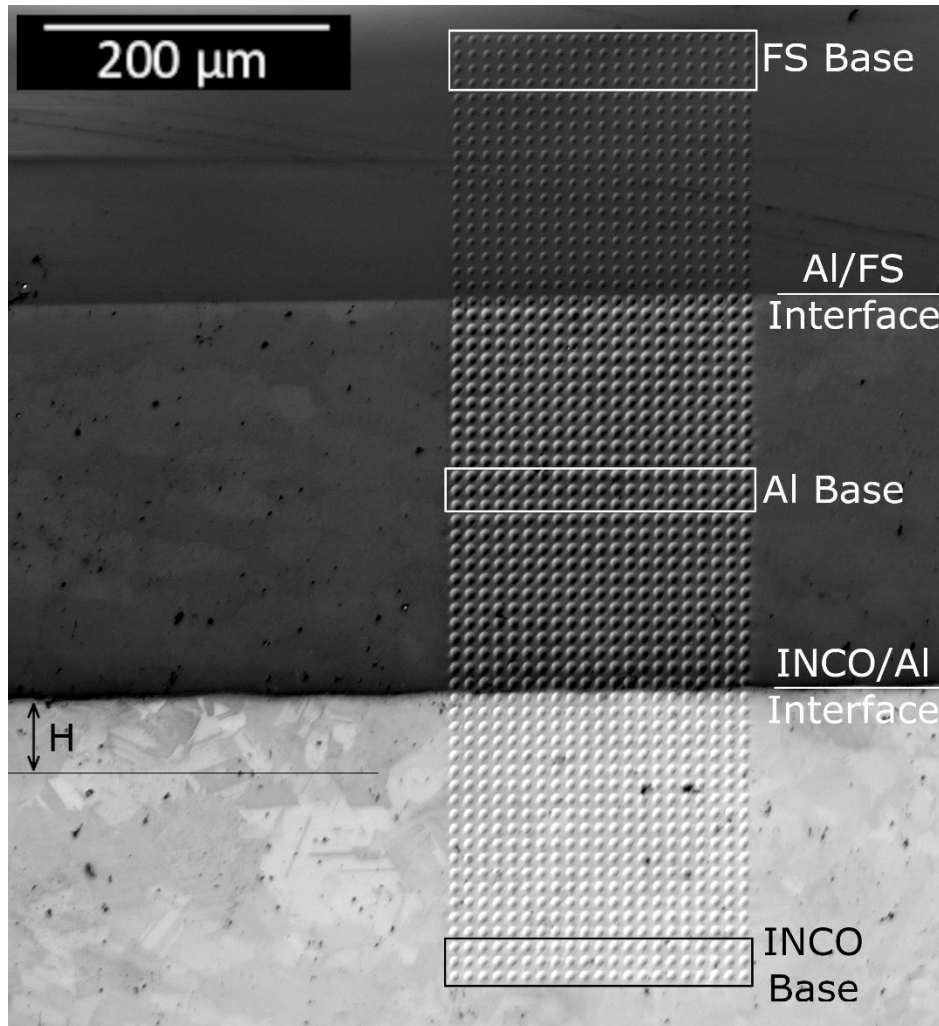


Figure 6: (a) BSE-SEM panoramic top view of Sample B after indentation mapping and (b) SE-SEM image of Sample A mounted on the ASA with a tilt of approximately 80°. Notice that in (b) the sample is rotated by 90° with respect to Figure 3b. Images taken with Zeiss DSM962 SEM.

A SE-SEM image of the mapped area in Sample A is shown in Figure 7, in which the grain structure of Inconel and aluminium is evident. Three regions sufficiently far away from the interfaces are defined as “base material”, for Inconel (INCO), aluminium (Al) and fused silica (FS), respectively. The black arrow (H) indicates a layer of 50  $\mu\text{m}$  near the INCO/Al interface in which the Inconel macrostructure

is considerably refined. Each spherical imprint performed with the 5  $\mu\text{m}$  tip is shown to be smaller than most of the grains in both materials.

SE-SEM higher magnification of indentation map in both INCO/Al and aluminium/FS interfaces in Sample B are shown in Figure 8.



*Figure 7:* SE-SEM image of a 5  $\mu\text{m}$  tip indentation map in Sample A. Definition of Inconel base (INCO-Base), aluminium base (Al-base), fused silica base (FS-base), Inconel/aluminium (INCO/Al) Interface, aluminium/fused silica (Al/FS) Interface and hardening (H) regions. Image taken with TESCAN MIRA3 SEM.

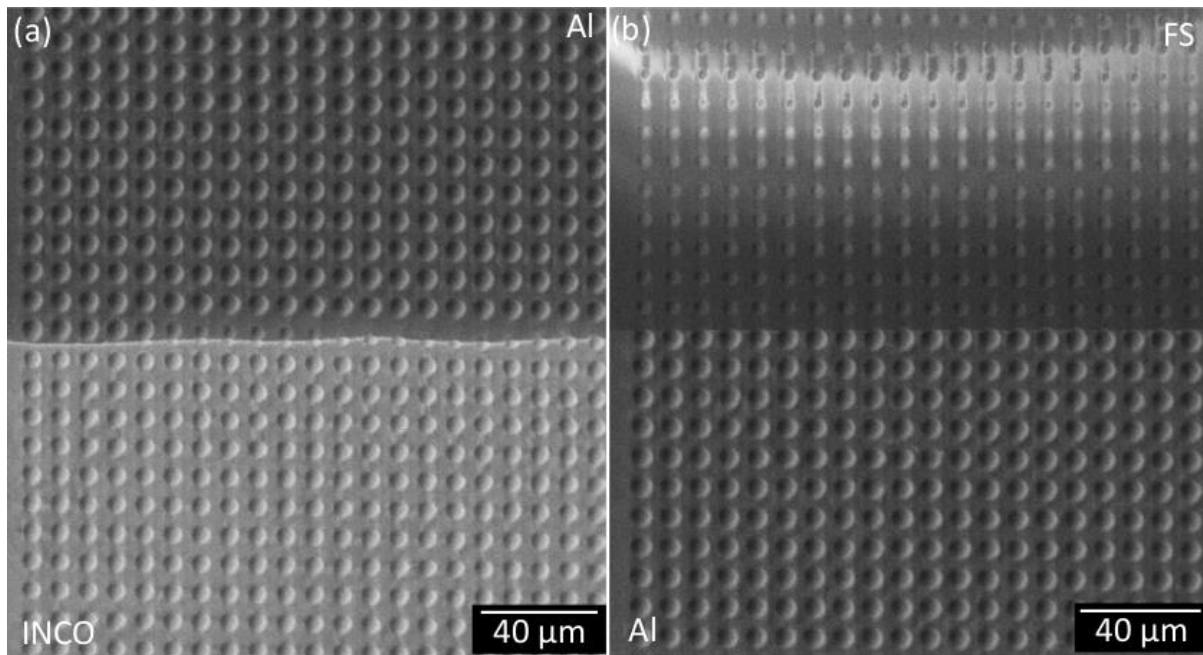


*Figure 8:* Close-up view of 5  $\mu\text{m}$  tip indentation map in both (a) INCO/Al and (b) Al/FS interfaces of Sample B. Notice the artefact due to electric charging in fused silica, top part of (b). Images taken with Zeiss DSM962 SEM.

Figure 9 shows a comparison between SE-SEM image, hardness map, elastic modulus map, yield stress map and yield strain map from different Samples A-D upon 5  $\mu\text{m}$  indentations. Notice that position (0,0) in the maps identifies the first imprint. As mechanical properties values considerably change from one material to another, colour ranges in the scale of each map have been manually adjusted to underline specific features in each material domain. There is a very good correlation between all maps and SEM images. Interestingly, hardness and yield stress maps show a considerable hardening in the Inconel near the INCO/Al interface in the so-called hardening (H) layer (see Figure 7). elastic modulus maps show a layer in the aluminium near the INCO/Al interface in which the elastic modulus is increased. Fused silica in Sample A and B shows constant and homogeneous mechanical properties, even very close to the Al/FS interface. Conversely, Sample C and D show perturbation in the FS (mainly appreciable in the elastic modulus maps). SEM images in Figures 10 and 11a show that in fused silica of both samples there are cracks, either at the Al/FS interface of Sample C (Figure 10) or perpendicular to it in Sample D (Figure 11a). Figure 11b shows a higher magnification of the Al/FS interface, where cracks propagate from an indent to another following a path parallel to the interface itself.

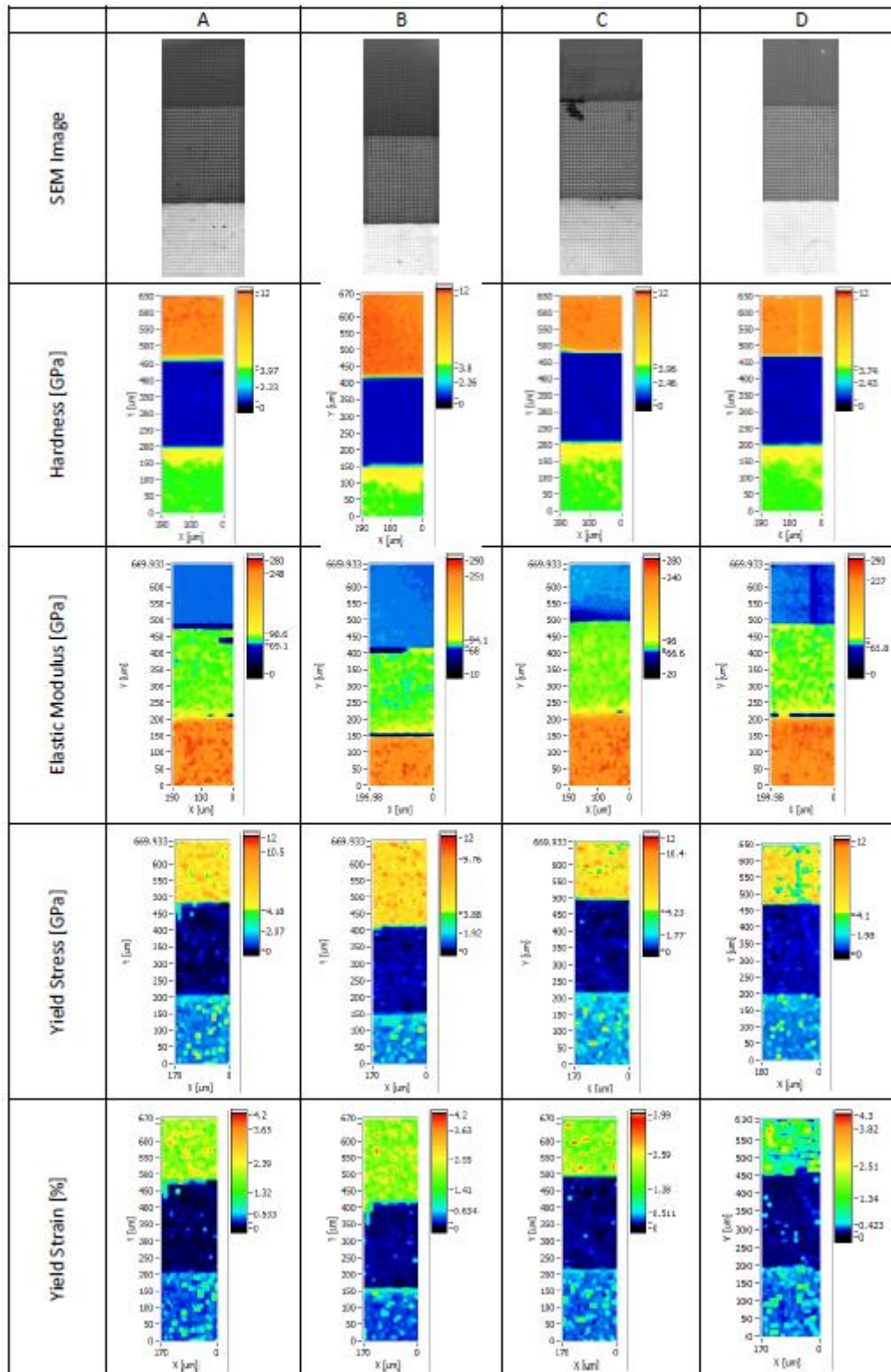


Figure 9: Comparison of SE-SEM images, hardness maps, elastic modulus maps, yield stress maps and yield strain maps of Samples A-D. SEM images take with TESCAN MIRA3 SEM.

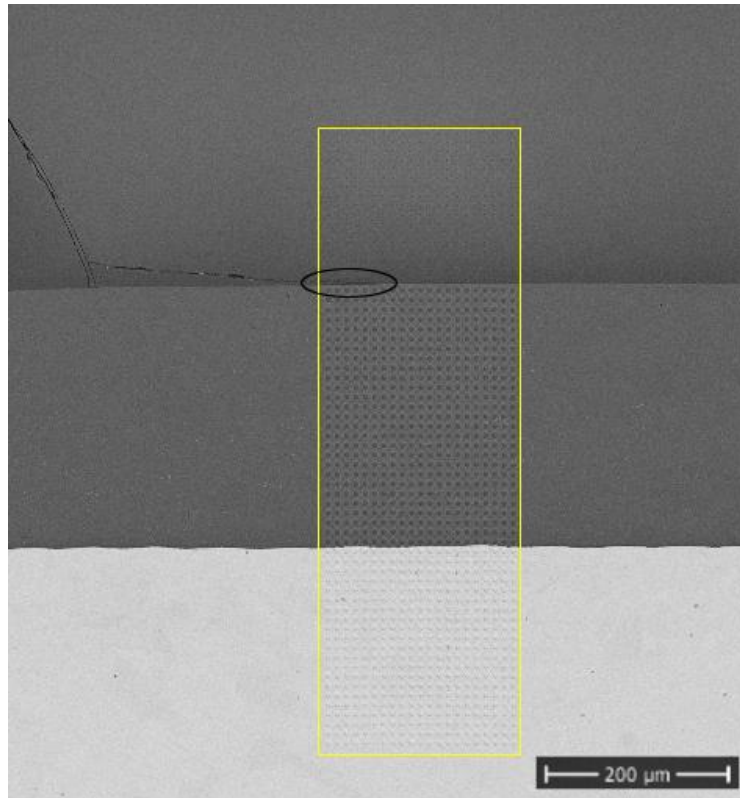


Figure 10: BSE-SEM image of an indentation map in Sample C. Image taken with Zeiss DSM962 SEM. Notice the cracks along the interfaces.

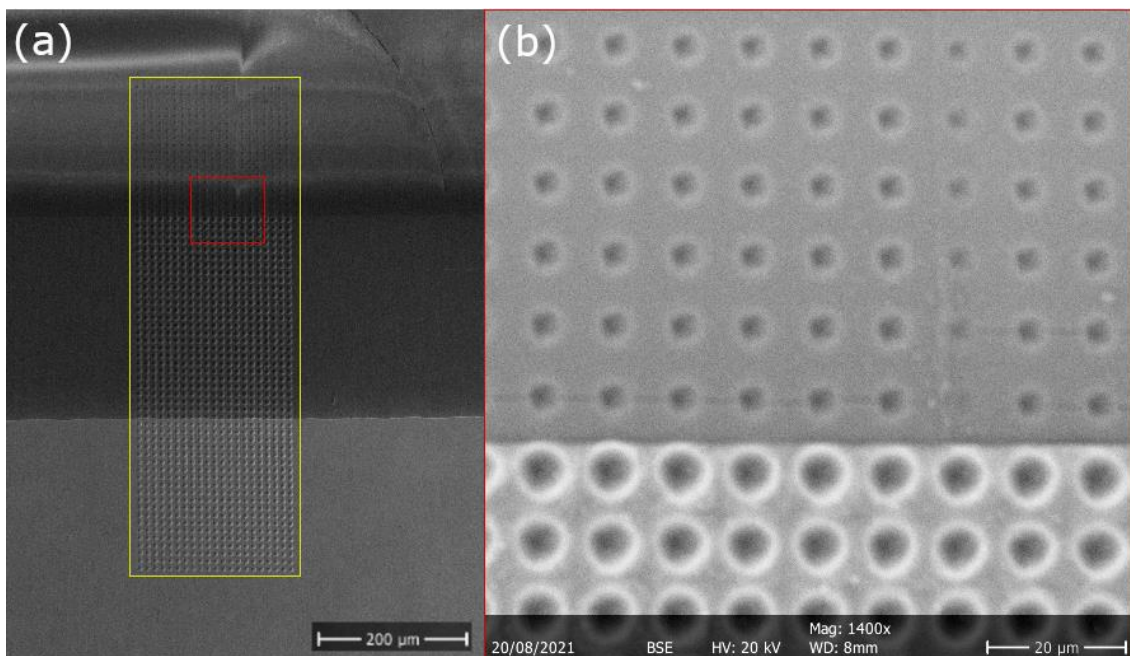


Figure 11: (a) SE-SEM image of a 5 μm tip indentation map in Sample D and (b) BSE-SEM at higher magnification of cracking at the Al/FS interface. Images taken with Zeiss DSM962 SEM.

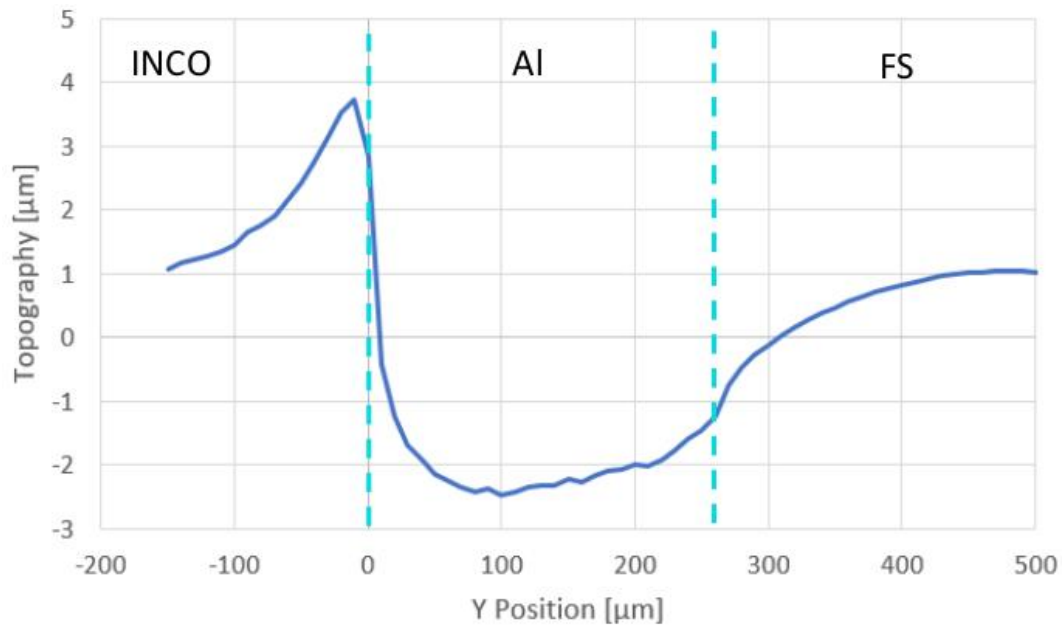


Figure 12: Typical topography profile plot of Sample B.

As each line of the indentation maps is parallel to the INCO/Al and Al/FS interfaces, properties map shown in Figure 9 can be easily translated in profile maps along the y axis, as shown in Figures 12, 13 and 14. In both figures, the solid line connects the mean values of each property in each specific line while the error bars account for twice the standard deviation (once on each end). Standard deviation in y position was smaller than  $0.0020 \mu\text{m}$ , its error bar is not shown for clarity. Notice that the INCO/Al interface has been arbitrarily selected as 0 position. Figures 13 and 14 also show a focus on the aluminium layer for clarity.

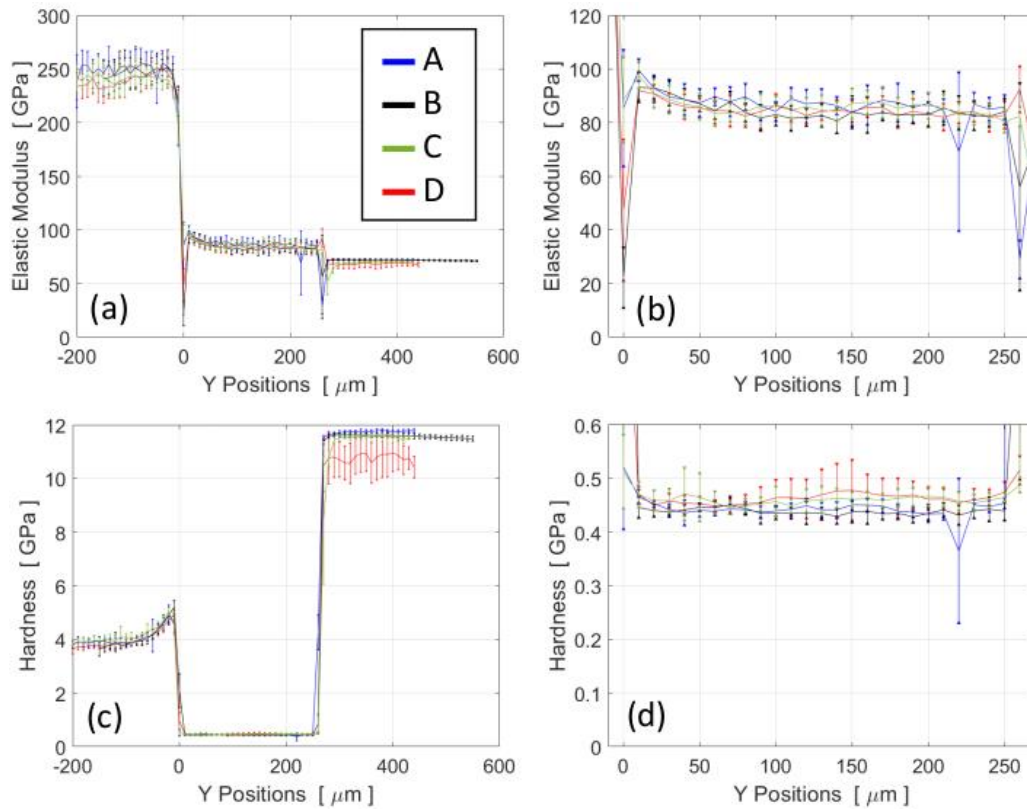


Figure 13: Profiles of mechanical properties from spherical nanoindentation mapping and subsequent stress-strain analysis using the 5  $\mu\text{m}$  spherical tip. (a) Elastic modulus, and (c) hardness of Samples A-D, displayed as profile plot along a path that is perpendicular to both INCO/Al and Al/FS interfaces. Values of each row of the map have been averaged (solid lines) and twice their standard deviation is displayed as error bars. Notice that the INCO/Al interface has been arbitrarily selected as 0 position. Details of elastic modulus and hardness of the aluminium layer (from 0 to 260  $\mu\text{m}$ ) are shown in (b) and (c), respectively.

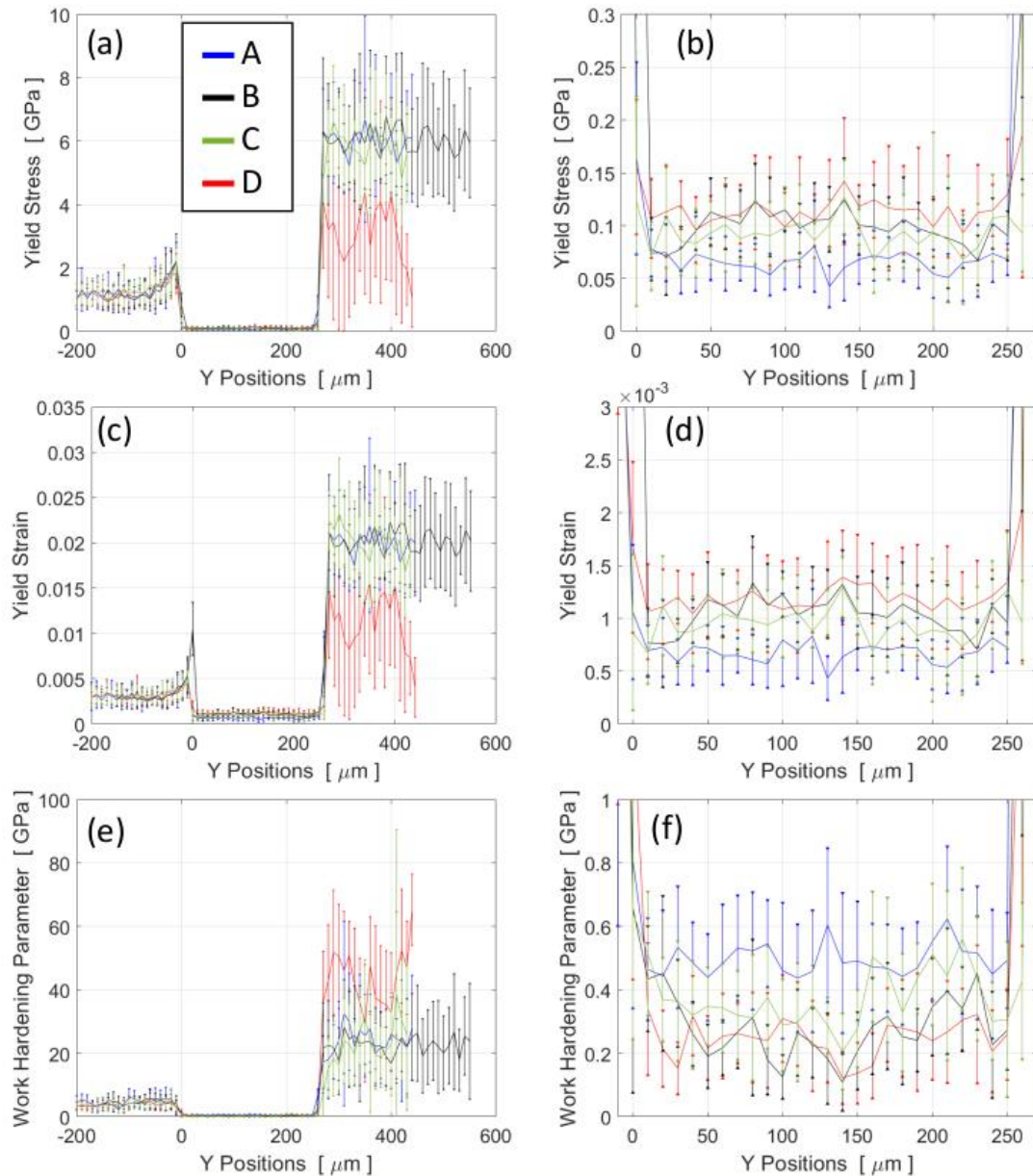


Figure 14: Profiles of mechanical properties from spherical nanoindentation mapping using the 5  $\mu\text{m}$  spherical tip and subsequent stress-strain analysis. (a) Yield stress, (c) yield strain and (e) work hardening parameter. Results of Samples A-D are displayed as profile plots along a path that is perpendicular to both INCO/Al and Al/FS interfaces. Values of each row of the map have been averaged (solid lines) and twice their standard deviation is displayed as error bars. Notice that the INCO/Al interface has been arbitrarily selected as 0 position. Details of profiles of aluminium layer (from 0 to 260  $\mu\text{m}$ ) are shown in (b), (c) and (d).

Figure 15 shows the indentation properties profile obtained by indentation map on Sample E and F using the 2  $\mu\text{m}$  tip. Similarly to Figures 13 and 14, a solid line connects the mean values of each property in each specific line while the error bars account for twice the standard deviation. The INCO/Al interface has been arbitrarily selected as 0 position.

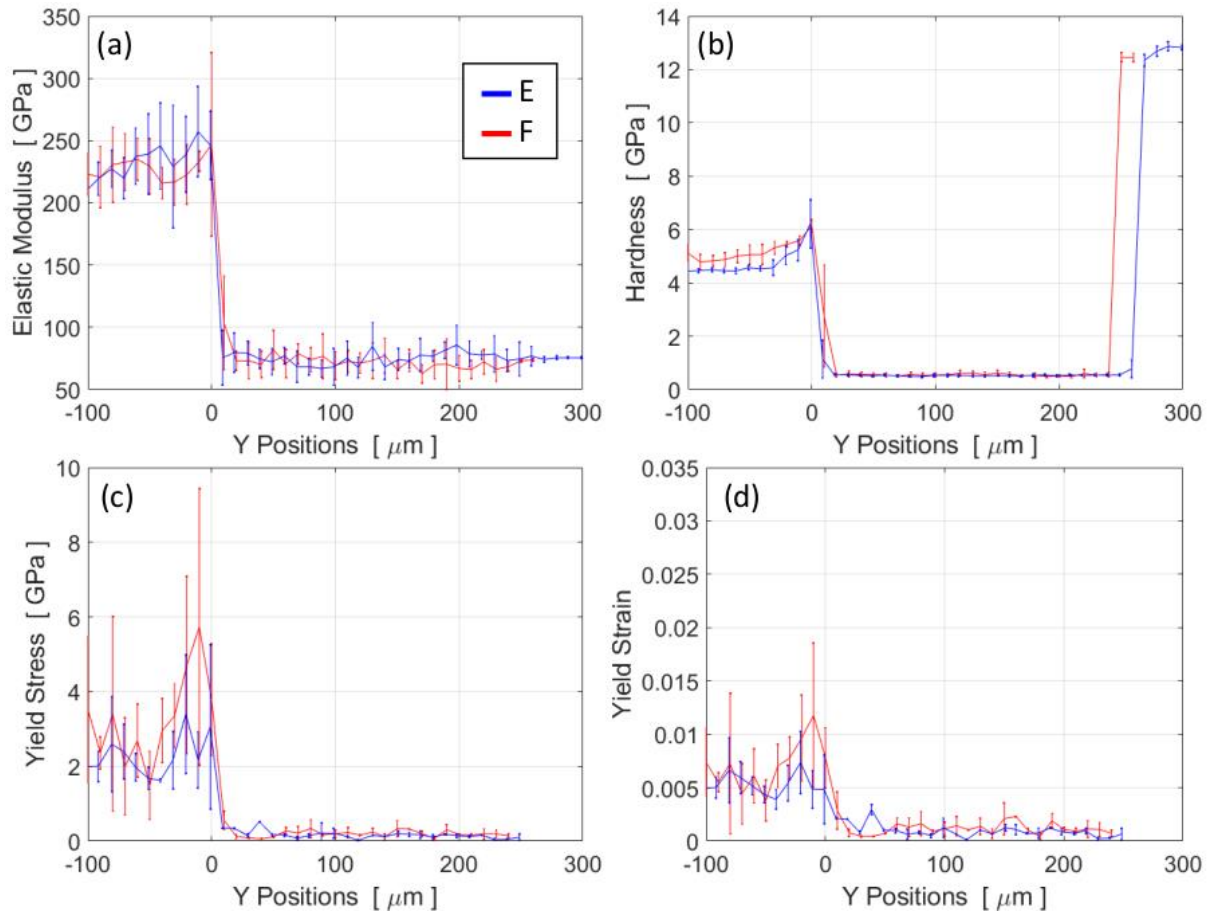


Figure 15: Profiles of mechanical properties from spherical nanoindentation mapping using the 2  $\mu\text{m}$  spherical tip and subsequent stress-strain analysis. (a) elastic modulus, (b) hardness, (c) yield stress and (d) yield strain. Results of Sample E and F displayed as profile plot along a path that is perpendicular to both INCO/Al and Al/FS interfaces. Values of each raw data point of the map have been averaged (solid lines) and twice their standard deviation is displayed as error bar. Notice that the INCO/Al interface has been arbitrarily selected as the 0 position.

Figure 16 shows the comparison of elastic modulus and hardness obtained using the three different indentation tips (*i.e.*, Berkovich, 2  $\mu\text{m}$  spherical, and 5  $\mu\text{m}$  spherical tips) in terms of property profiles and cluster plots. Figure 17 shows the comparison of yield stress and yield strain profile plots performed with both 2  $\mu\text{m}$  and 5  $\mu\text{m}$  tips. The INCO/Al interface has been arbitrarily selected as the 0 position in the profile graphs in both Figures 16 and 17.

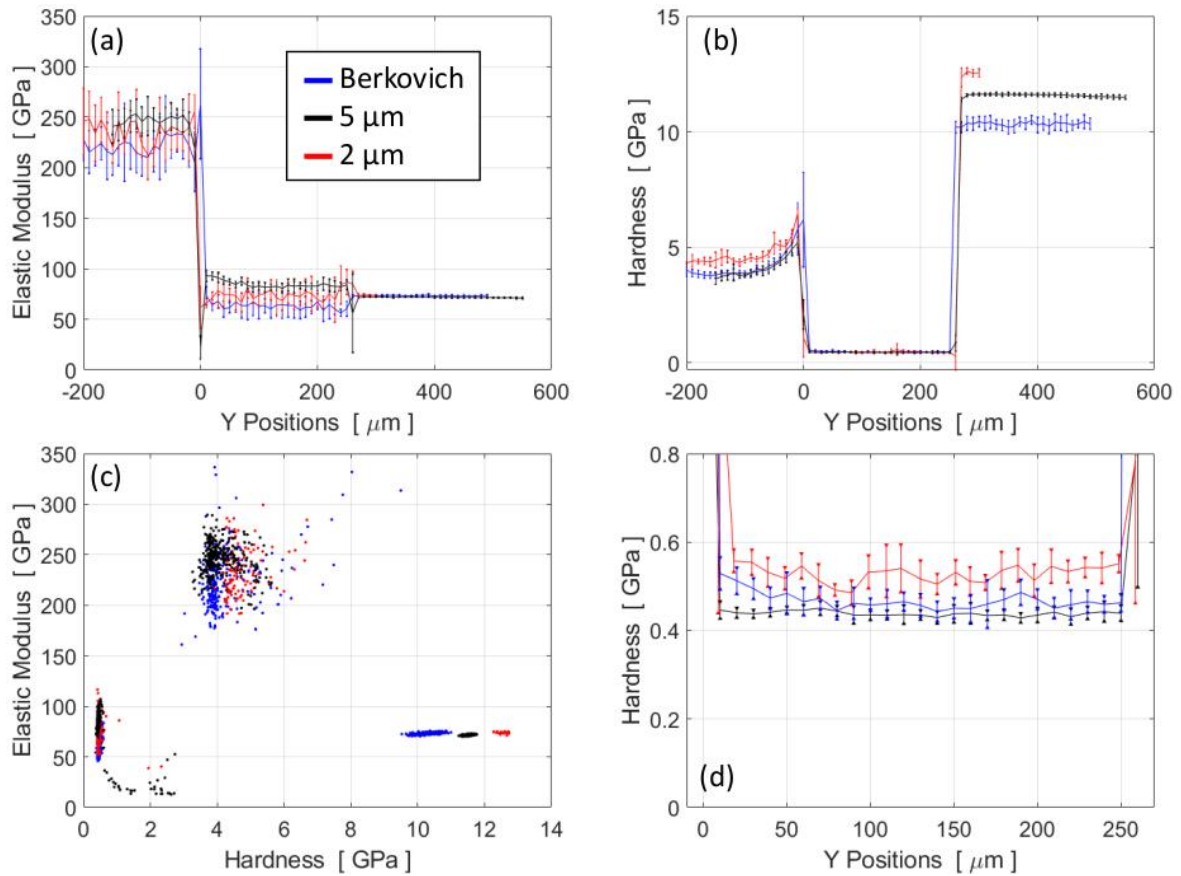


Figure 16: Comparison of indentation results obtained from different tips, namely, Berkovich, 2  $\mu\text{m}$  spherical and 5  $\mu\text{m}$  spherical. Results are compared in terms of (a) elastic modulus, (b) hardness and (c) cluster plots. Details of hardness profile in the aluminium layer are shown in (d).

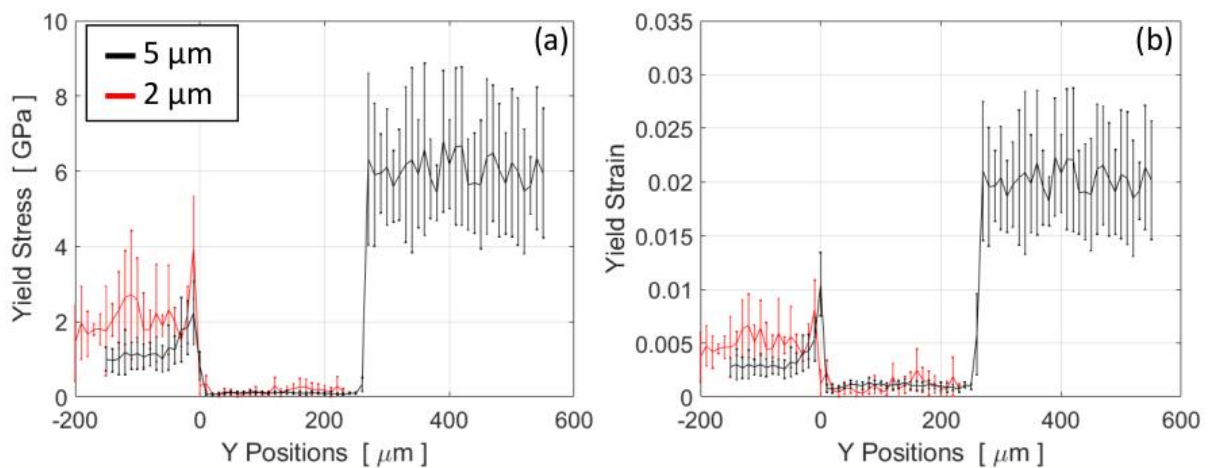


Figure 17: Comparison of indentation Stress-Strain results obtained from 2  $\mu\text{m}$  and 5  $\mu\text{m}$  tips. Results are compared in terms of (a) yield stress and (b) yield strain profile plots.

Mean and standard deviation values of hardness, elastic modulus, Yield stress, Yield Strain and Work Hardening Parameter are listed in Table 1.

Table 1: summary of indentation results from different samples and different indentation tips.

Sample	Tip	Location	Hardness [GPa]		Elastic Modulus [GPa]		Yield Stress [GPa]		Yield Strain		Work Hardening Parameter [GPa]	
			mean	SD	Mean	SD	Mean	SD	Mean	SD	Mean	SD
A	5 $\mu$ m	INCO-Base	3.9	0.2	248	17	1.2	0.4	0.0030	0.0012	4.4	1.9
		Al-Base	0.44	0.01	87	4	0.07	0.03	0.00067	0.00035	0.5	0.2
		FS-Base	11.8	0.1	72.0	0.3	6.0	1.8	0.0199	0.0055	24.1	13.5
B	5 $\mu$ m	INCO-Base	3.8	0.2	246	16	1.0	0.4	0.0028	0.0011	4.2	2.1
		Al-Base	0.43	0.01	82	4	0.11	0.03	0.00116	0.00032	0.2	0.1
		FS-Base	11.6	0.1	71.6	0.5	6.1	1.7	0.0203	0.0052	22.4	12.3
C	5 $\mu$ m	INCO-Base	3.9	0.2	241	12	1.2	0.4	0.0032	0.0011	3.7	1.7
		Al-Base	0.46	0.02	85	4	0.10	0.03	0.00107	0.00030	0.3	0.1
		FS-Base	11.5	0.1	70.4	0.5	5.8	1.8	0.0198	0.0057	25.2	23.7
D	5 $\mu$ m	INCO-Base	3.7	0.1	235	12	1.2	0.4	0.0032	0.0010	3.4	1.4
		Al-Base	0.47	0.04	85	4	0.12	0.05	0.00121	0.00044	0.2	0.1
		FS-Base	10.8	0.7	68.6	3.1	3.3	2.5	0.0120	0.0083	43.7	20.0
B	2 $\mu$ m	INCO-Base	4.5	0.1	215	15	2.2	1.1	0.0056	0.0025	-	-
		Al-Base	0.45	0.05	74	11	0.15	0.11	0.00095	0.00071	-	-
		FS-Base	12.4	0.1	74	1	-	-	-	-	-	-
E	2 $\mu$ m	INCO-Base	4.4	0.2	213	19	1.9	0.4	0.0049	0.0008	-	-
		Al-Base	0.52	0.04	74	13	0.14	0.07	0.00083	0.00046	-	-
		FS-Base	12.9	0.1	75.6	0.6	-	-	-	-	-	-
F	2 $\mu$ m	INCO-Base	5.0	0.3	221	19	3.4	1.7	0.0072	0.0027	-	-
		Al-Base	0.6	0.1	73	11	0.22	0.12	0.00137	0.00081	-	-
		FS-Base	-	-	-	-	-	-	-	-	-	-
B	Berko	INCO-Base	3.9	0.2	220	22	-	-	-	-	-	-
		Al-Base	0.46	0.02	63	10	-	-	-	-	-	-
		FS-Base	10.3	0.3	73	1	-	-	-	-	-	-

## 6 Discussion

All indentation maps, regardless the indenter shape, show that the mechanical properties of the 3 different materials at a distance from interfaces and defects are constant. Note that especially the elastic modulus of fused silica shows good reproducibility, not only in terms of scatter of results within one single map, but also in terms of quantitative comparison between all samples, indenter tip shapes and indentation protocols. Only the mechanical properties of the fused silica base material in Sample D markedly deviates from other samples (see red curves in Figures 13a, 13c, 14a, 14b and 14c). This is mainly due to the large crack observed in Figure 11. The otherwise outstanding repeatability indicates that i) different diffusion bonding processes have not altered the elastic modulus of the fused silica base material, ii) sample preparation was optimal and repeatable among different samples, iii) system compliance is independent on the mounted sample and tip and iv) wear of tip had negligible impact on measurements even after several thousand of indentations. In other words, results on fused silica constitutes a common background between the different samples and experimental conditions

offering a unique and convenient tool for the quantitative comparison of mechanical performance across the diffusion bonded joints.

The mechanical properties such as the elastic modulus of both aluminium and Inconel (Figure 16) is characterized by a larger scatter compared to the elastic modulus of fused silica. Figure 7 reveals that the average grain size in both aluminium and Inconel is larger than the imprint left by the 5  $\mu\text{m}$  tip. The relatively large scatter observed across this microstructure is believed to originate from this heterogeneous microstructure [14] [9]. It is known that the elastic modulus of aluminium can change up to 15.9% depending on the crystallite orientation [22] [23].

Furthermore, the elastic modulus as well as hardness, yield stress, and yield strain values of both aluminium and Inconel exhibit to some extent a tip shape dependence (Figure 16a). This is in agreement with literature [4] [24] [25]. Interestingly, this dependence of mechanical properties on the indenter shape is more pronounced in fused silica than in aluminium and Inconel as shown in Figures 16 and 17. The mean yield stress of fused silica in the range 5.8–6.1 GPa measured here with the 5  $\mu\text{m}$  tip (Table 1) is in good agreement with the value of  $6.5 \pm 1$  GPa in ref. [4] for an analogous fused silica sample using an analogous spherical indentation stress-strain methodology. The yield stress value found here matched also well with the values between 6.5 and 7 GPa reported in a number of studies based on fused silica micropillar compression [26] [27] [28].

The work hardening parameter (Figure 14e) is defined here as the slope of the linear elastoplastic stress-strain curve (see Figure 5b). Material hardening often has a linear trend when subjected to spherical indentation [4] [6]. Table 1 and Figure 14e shows that Inconel has considerably larger work hardening capability than pure aluminium, which is in agreement with tensile test results from the literature [29] [30]. Moreover, fused silica exhibits considerably larger work hardening parameter than both aluminium and Inconel, which is in agreement with spherical indentation stress-strain analysis on pure aluminium and fused silica [4] and with micropillar compression results of fused silica [31] [32], which also show remarkable hardening.

Hardness maps in Figure 9 show that there is a layer of approximately 50-100  $\mu\text{m}$  in the Inconel near the INCO/Al interface that exhibits considerably larger hardness. The same layer is also characterized by increased yield stress and yield strain as shown in Figures 14a and 14c. Incidentally, topography maps shows that the topological level of such hardened layer is few micrometres higher than in the surrounding aluminium and base-Inconel materials (Figure 12). This is a typical artefact in dissimilar joints due to different wear rate of materials composing the joint during polishing, which occurred here even though care has been taken during polishing [33]. Notice that there is no change in elastic modulus in the same region, thus, the difference in hardness cannot be explained by an error in the projected contact area estimation due to the non-perfectly flat surface. It is believed that such a relatively harder layer in the Inconel is mainly due to microstructure transformations at the interface. Incidentally, Figure 7 (H layer) shows that the Inconel microstructure at the INCO/Al interface is characterized by a smaller grain size richer in twin boundaries compared to the base material. Analogous grain refinement was observed in a similar Inconel718-Inconel718 [34] diffusion bonded joint, while both grain refinement and twinning were detected in a dissimilar Inconel625-AISI4130 [35] diffusion bonded joints. Both papers [34] [35] pointed out that also marked carbide precipitation can take place in the Inconel. It cannot be excluded that analogous precipitation has taken place here, which would result in a further contribution to increased hardness in the Inconel near INCO/Al interface.

Previous investigation carried out by some of the Authors [3] on analogous diffusion bonded joints pointed out that modifications of the chemical composition across the aluminium/Inconel is limited

to an interdiffusion layer of maximal 10  $\mu\text{m}$  in thickness. As the layer of increased hardness here is considerably larger (50-100  $\mu\text{m}$ ) than such interdiffusion layers it is concluded that this is not a result of a variation in chemical composition of the interdiffusion layer. On the other hand, the maps obtained with the 5  $\mu\text{m}$  tip and the corresponding mechanical properties profiles show that, at the INCO/Al interface, elastic modulus of Inconel and aluminium are slightly smaller and larger, respectively, compared to the base materials (Figures 9, 13a, 13b and 16a). These layers of altered elastic moduli extend about 20  $\mu\text{m}$  into the Inconel side and up to 40  $\mu\text{m}$  into the aluminium side, which is again considerably larger than typical chemical interdiffusion layers [3]. Unlike the layer of increased hardness though, the layers of altered elastic moduli developed asymmetrically on both sides of the INCO/Al interface. It must be kept in mind that the elastic volume involved by a single nanoindentation can be considerably larger than the elastoplastic volume [36], thus indentation modulus can be sensitive to a perturbation in the material that is at a relatively large distance from the indentation itself. Even if the quantification of this volume is challenging and beyond the scope of the present paper, it is reasonable to expect that a 1.5  $\mu\text{m}$  maximum depth indentation (using 5  $\mu\text{m}$  tip) performed 40  $\mu\text{m}$  away from the INCO/Al interface is affected by a perturbation in the chemical composition at the interface. Incidentally, the results from indentations with the Berkovich tip and 2  $\mu\text{m}$  spherical tip at much shallower indentations (maximum depth of approximately 600 nm) are characteristic of a considerably smaller elastic volume, and, thus, profiles in Figures 15a and 16a do not clearly show any elastic modulus affected layer.

Elastic modulus mismatch between aluminium and fused silica is almost zero, therefore, no layer of affected elastic modulus is observed at the Al/FS interface (see for instance elastic modulus maps and profiles in Figures 9 and 13, respectively, for both Samples A and B). Completely different behaviour can be observed in Sample C, where a marked gradient in elastic modulus is detected in a layer of about 50  $\mu\text{m}$  on the fused silica side. However, Figure 10 shows that a crack on the fused silica propagates at the Al/FS interface of Sample C. The abnormal elastic modulus gradient in the sample is due to loss of bonding between aluminium and fused silica at their interface. It is interesting to note that there is no change in elastic modulus on the aluminium side, indicating that most of residual stress is concentrated in the fused silica, in agreement with previous observation on analogous diffusion bonded joints [3].

The diffusion bonded joints under study are well-known to contain some subcritically-sized cracks [3] and it is believed here that growth and propagation of those cracks has occurred during sample preparation (cutting and polishing), when mechanical solicitation is far more intense than during the normal in-service solicitation of the component. In other words, cracks in both Sample C and D are not characteristic of the in-service performance of the diffusion bonded joint but offer a unique opportunity to test and validate the present methodology. For instance, from a visual inspection of Sample C (Figure 10), the crack seems to stop in the area highlighted with a black circle, while the remaining interface looks undamaged. Indeed, as already discussed before, the map of the elastic modulus clearly shows that debonding occurred along the entire mapped area and not only in the black circled area. The here proposed methodology is therefore able to detect a crack even when it can be overlooked from a visual inspection. This consideration, in turn, gives *a posteriori* confirmation that maps performed on all the other samples (other than Sample C and D) were performed at sufficient distance from any defect, visible or not, and their results are then characteristic of the bonded joint performance.

## 7 Conclusions and Future Outlook

A novel methodology based on dynamic spherical nanoindentation has been proposed to map tensile-like mechanical properties of materials at the micro- and nano-scales, including yield stress, yield strain, work hardening parameter and elastic modulus. The methodology takes inspiration from the well-known theory to extract stress-strain curves from spherical nanoindentation applied to automated large map and relies on a fully automated post-processing protocol. The methodology has been applied to 3 very different materials, namely, aluminium, Inconel 625 and fused silica, joined by diffusion bonding. Results from the present study will be used for the qualification of material assemblages for observation windows in the ITER fusion reactor. The tensile-like mechanical properties will be used in three-dimensional FEM simulations to predict the mechanical behaviour of the bonded joints.

The method has proven to be very versatile as one single indentation protocol applies to materials of very different in nature (metals and ceramics). The presence of fused silica in the samples enables a common reference between different samples. This allowed a reliable and quantitative comparison of resulting data. The results show a marked layer of increased hardness at the Inconel/aluminium interface, which has been related to twinning and microstructure refinement. The presence of high residual stress located at the aluminium/fused silica interface has been confirmed. Finally, as the in-service temperature of the windows is at extreme temperatures, an analogous investigation at high temperature should be performed to improve FEM predictions on in-service performance.

## 8 Declaration of Competing Interest

The authors declare that they have no known competing financial interests or personal relationships that could have appeared to influence the work reported in this paper.

## 9 CRediT authorship contribution statement

**R. Pero:** Investigation, Writing – original draft, Data curation, Formal analysis, Methodology, Visualization, Video. **N. Randall:** Project administration, Conceptualization, Methodology, Writing – original draft, Supervision. **D. Frey:** Software Development, Formal analysis, Methodology, Writing – review & editing, Data curation, Validation. **R. Widmer** Writing – original draft, Investigation, Imaging, Writing – review & editing. **T. Darby:** Visualization, Writing – original draft, Investigation. **L. Aucott:** Project administration, Funding acquisition, Writing – original draft, Supervision, Conceptualization. **C. Hardie:** Writing – review & editing, Supervision. **S. Pak:** Validation, Writing – review & editing, Supervision, Conceptualization, Project administration. **P. Maquet:** Validation, Writing – review & editing, Supervision. **A. Bushby:** Methodology, Conceptualization, Supervision, Writing – review & editing, Validation.

## 10 Acknowledgements

This work was supported by the ITER Organization through the framework contract (6000000117). The views and opinions expressed herein do not necessarily reflect those of the ITER Organization. Thanks to Dr. Xavier Maeder and Dr. Amit Sharma from EMPA for providing GaAs and sapphire reference samples. Thanks Prof. Johannes Michler from EMPA for imaging analysis on TESCAN MIRA

3 SEM. Thanks Edgar Tommasini from Alemnis AG for help with Figure 3. Thanks Dr. Robbie McLauchlan from UKAEA for providing images for Figures 1 and 2.

## Appendices

### APPENDIX A (Tip area calibration procedure and data)

Tip area calibration (TAC) is a procedure to determine the projected contact area vs contact depth relationship of an indenter. The procedure consists in the measurement of the contact stiffness versus contact depth relationship ( $C_s(h_c)$ ) in a reference material with known elastic modulus and Poisson's ratio. The real projected contact area vs contact depth relationship can be calculated using the following equation [16]:

$$E_s = \frac{1 - \nu_s^2}{\frac{2 \cdot C_s(h_c) \cdot \sqrt{A_p(h_c)}}{\sqrt{\pi}} - \frac{1 - \nu_i^2}{E_i}} \quad \text{Eq. A.1}$$

where the real projected contact area versus the contact depth relationship can be expressed by the following equation [19] [16]:

$$A_p(h_c) = \sum_{i=0}^8 c_i * h_c^{2^{i-1}} \quad \text{Eq. A.2}$$

For Berkovich indenter  $c_0 = 24.5$  [16] [19], while for a spherical indenter  $c_0 = \pi$  and  $c_1 = 2\pi R$  [5]. All the other  $c_i$  coefficients have been determined by the TAC procedure.

The employed methodology can be applied provided that: i) the elastic modulus and Poisson's ratio of both indenter tip and reference material are known, ii) the reference material exhibits limited indentation size effect (ISE), iii) the reference material exhibits limited strain rate sensitivity, iv) the frame compliance of the machine is known.

In the present study, the contact stiffness vs contact depth relationship has been obtained through continuous stiffness measurement (CSM) with 10 Hz oscillation frequency. A Berkovich indenter has been calibrated on a fused silica reference block by means of 3 CSM nanoindentations.

As the stress strain analysis is highly sensitive to the TAC, each spherical indenter (2 and 5  $\mu\text{m}$ ) has been calibrated on 4 different reference materials, namely, fused silica, Si(100), GaAs(100) and Sapphire. A minimum of 3 CSM indentations have been performed in each case. TAC functions of the 2 spherical indenters for the 4 reference materials are shown in Figure A.1. The results from different reference materials are in good agreement for both indenters.

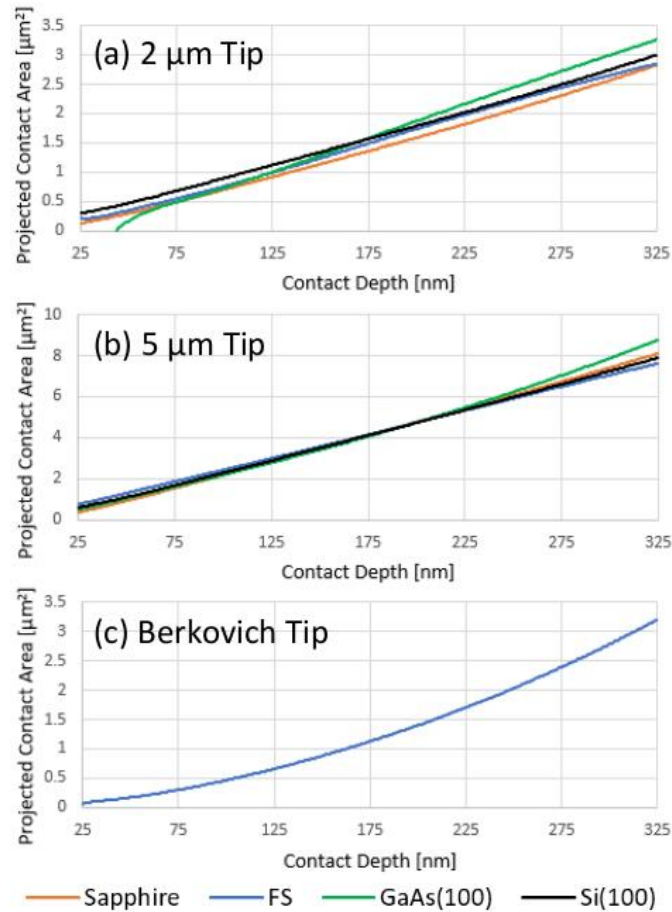


Figure A.1: Tip Area Function (TAC) obtained from 4 reference samples (fused silica, Si(100), GaAs(100) and Sapphire) for (a) the 2 and (b) 5  $\mu\text{m}$  tips. (c) TAC obtained from FS reference sample for the Berkovich tip.

## APPENDIX B (Influence of indentation spacing on the results)

Spacing is an important parameter in indentation mapping, as a smaller spacing will give a higher spatial resolution, but if too close to each other one indentation may influence its nearest neighbours and therefore affect the indentation results. According to the ISO14577-1 standard, the minimum spacing between 2 indentations is either 3 times the indentation diameter or 10 times the maximum indentation depth, whichever is greater. However, the authors experience suggests that in many materials the error induced by a smaller spacing is negligible compared to the scatter in indentation properties at the nano- and micro-scale. This is supported by a systematic investigation based on indentation mapping [37] which shows that a spacing of 10 times the maximum indentation depth is a sufficient spacing in mapping for Berkovich indents in a number of materials (including aluminium, nickel and fused silica, that are the main players in the current study), regardless of the indentation diameter. Note that for a Berkovich indent, the indentation diameter is approximately 7 times the maximum depth and according to the current ISO14577 standard, the minimum spacing between indentations should be approximately 21 times the maximum depth which is double the value proposed in reference [37].

In the present paper, a minimum spacing of 10  $\mu\text{m}$  has been selected for all the indenters, namely, Berkovich and both the 2  $\mu\text{m}$  and 5  $\mu\text{m}$  spherical indenters.

The maximum depth on Berkovich indentation was approximately 600 nm, thus the theoretical minimum spacing of 6  $\mu\text{m}$  (according to [37]) is considerably smaller than the selected 10  $\mu\text{m}$ .

For spherical imprints, which is the main focus of the present study, the spacing between imprints has been investigated carefully during preliminary tests. In the case of a 2  $\mu\text{m}$  imprint, the maximum depth was approximately 500 nm. Three indentation maps have been performed in the same area, progressively reducing the imprint spacing from 10  $\mu\text{m}$  to 5  $\mu\text{m}$  (see Figure B.1). First, a 6x51 indents map (Map A) with a spacing of 10  $\mu\text{m}$ , then a second map (Map B) having 5x51 indents with spacing of 10  $\mu\text{m}$  has been performed between the imprints of the first map. The result is an overall 11x51 indentation map with 10  $\mu\text{m}$  spacing in y and 5  $\mu\text{m}$  spacing in x. Finally, a third map (Map C) having 11x50 imprints and a spacing of 5  $\mu\text{m}$  in x and 10  $\mu\text{m}$  in y has been performed between the imprints of the first and second maps. The result is an overall map of 11x101 indentation map with a spacing of 5  $\mu\text{m}$  in both x and y. This is a convenient way to compare indentation properties as a function of the indentation spacing excluding the uncertainty due to mapping in different areas and have been achieved thanks to the very high precision of the x and y translations stages of the Alemnis ASA with a repositioning accuracy of 50 nm. Figure B.1 shows elastic modulus and hardness vs distance from the INCO/Al interface for the 3 maps having different spacing. Results shows virtually no difference, indicating that the selected 10  $\mu\text{m}$  spacing is suitable.

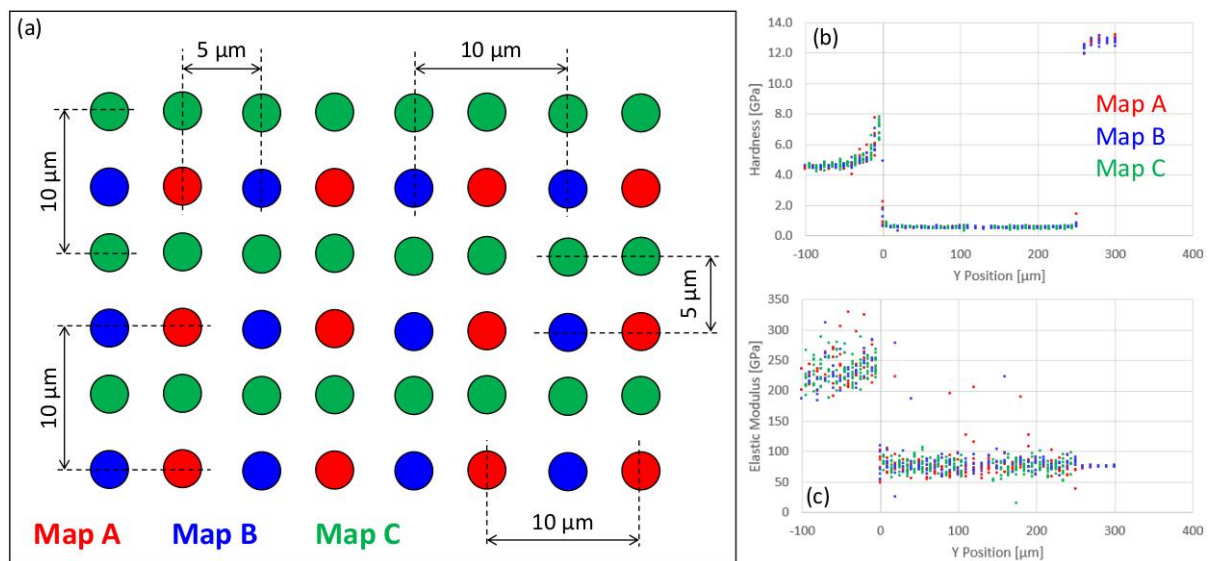


Figure B.1: (a) A out of scale sketch of 3 overlapped maps where each circle represents a spherical imprint. Comparison of indentation results: (b) elastic modulus and (c) hardness obtained from 3 maps having different indentation spacing performed with 2  $\mu\text{m}$  tips in the same area.

Effect of spacing on indentation results has also been investigated on Sample A using the 5  $\mu\text{m}$  tip. No difference in indentation results was detected reducing the spacing from 30  $\mu\text{m}$  to 10  $\mu\text{m}$  (results are not shown). This indicates that the selected 10  $\mu\text{m}$  spacing is suitable for the 5  $\mu\text{m}$  tip. An SEM Video of the map having 30  $\mu\text{m}$  spacing is attached to the present paper (Video 1).

Moreover, all indentation results reported in the present paper show no systematic difference between indentation results from indentation having different neighbourhood. For example, the first indentation of the map has not any surrounding indentations when it is performed, while all the other indentations on the first line have only one single indentation in their neighbourhood, all the first indentations of a new line have 2 indentations on their neighbourhood, and any other indentation has 3 indentations on their neighbourhood, but no remarkable difference in indentation properties was identified. This provides *a posteriori* confirmation that the spacing of 10  $\mu\text{m}$  selected in the present paper has no influence on the indentation results.

#### **APPENDIX C (Influence of indentation direction in map)**

The impact of the indentation direction on the results has been analysed as well. Most of the indentation maps discussed in the present paper have been performed starting from the Inconel, at a minimum distance of 150  $\mu\text{m}$  from the INCO/Al interface, progressing toward the fused silica. In this section 2 maps composed of 6x61 indentations with a spacing of 10  $\mu\text{m}$  have been performed on the same Sample B using the 2  $\mu\text{m}$  tip, the first one starting from the Inconel toward the fused silica and the second one starting from the fused silica to the Inconel. The results (Figure C.1) show that there is no difference between the 2 maps in terms of hardness, elastic modulus, yield stress and yield strain.

In the number of indentation maps shown in the present study, there is only one piece of evidence that suggests a possible influence of indentation direction on results, which is the map on Sample D (see Figures 9 and 11 as reference). As already discussed in the *Discussion* section, the first 2 lines of map in the fused silica near the Al/FS interface show that there is propagation of a crack between on imprint and another. However, crack propagation has not been observed in any other indentation map. Moreover, SEM image shows that the mapped area in Sample D has a crack that seems not related to the indentation process. It is therefore believed that the reason for such abnormal behaviour in terms of crack propagation between imprints has been originated by the crack present in the mapped area. Indentation direction might have played a role in the crack propagation, but it is not the main cause.

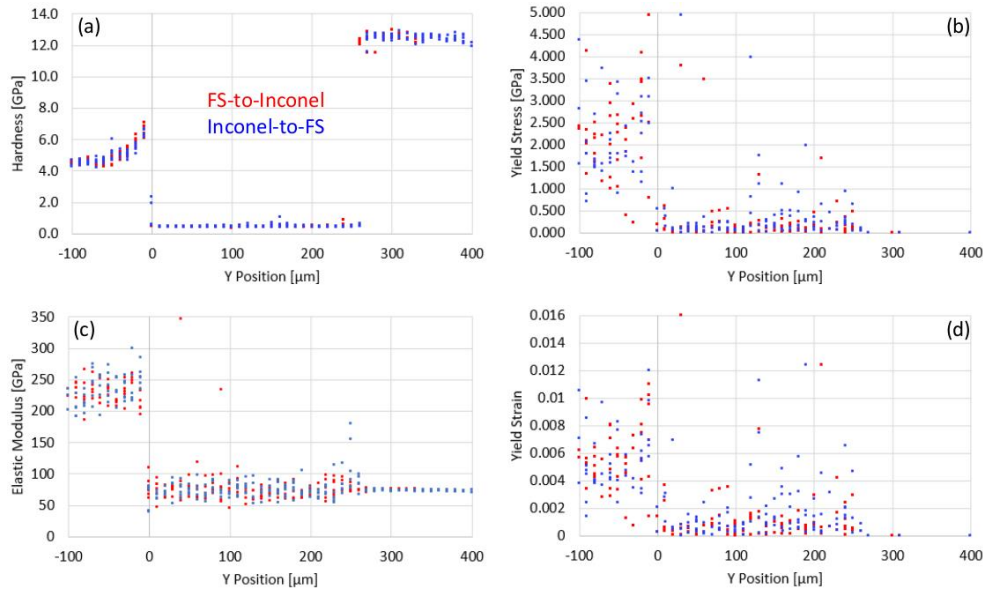


Figure C.1: Comparison of indentation results. (a) Hardness, (b) yield stress, (c) elastic modulus and (d) yield strain, obtained from 2 different mapping paths using the 2  $\mu\text{m}$  tip. One from Inconel to fused silica and another one from fused silica to Inconel.

#### APPENDIX D (Comparison of sinus to multicycle indentation in terms of size effect with a Berkovich indenter)

The indentation size effect (ISE) is a common phenomenon affecting indentation results. It occurs when indentation properties of a material have a marked depth dependence. The reasons behind such a behaviour are manifold and still being investigated. For instance, it may depend on the non-ideal indenter tip shape, sample preparation (superficial damaging, impurities, oxidation and residual stress), or even on the nature of the sample material itself, such as microcrystalline structure and deformation mechanism.

In order to quantify the ISE two main approaches have been selected in the present paper, both of them based on Berkovich indentation. The ISE analysis has been focused on aluminium and Inconel, as fused silica is well known to be almost free from ISE. All indentations were performed at a distance from the diffusion bonded interfaces.

The first approach consisted in performing a set of indentation with variable maximum depth between 100 and 1000 nm on each target material. Constant loading and unloading displacement rate of 100 nm/s, and no holding time have been imposed for all indentations. A number of 5 indentations at each depth have been performed on Inconel while 10 indentations have been performed on aluminium. Unloading analysis allowed to extract indentation properties and to build a hardness and elastic modulus vs contact depth graph.

The second approach was based on CSM indentation at 10 Hz frequency. The loading segment has been defined in displacement control at a constant strain rate of  $10^{-2} \text{ s}^{-1}$ . Each CSM indentation intrinsically provide a hardness and elastic modulus vs contact depth relationship. Three indentations have been performed on each material.

Figure D.1a and D.1b show that indentation curves at different maximum depth on aluminium and Inconel, respectively. It is interesting to see the good agreement of the individual loading curves. On

aluminium, the scatter of results seems to be slightly larger than in the case of Inconel, however, for a similar maximum depth, the maximum load in aluminium is considerably smaller than in Inconel, thus a larger apparent scatter in the indentation curves translates in a comparable relative standard deviation in terms of hardness and elastic modulus (see Figures D.1c, D.1d, D.1e and D.1f).

Both hardness and elastic modulus vs contact depth for both materials exhibit a plateau for contact depths larger than 550 nm (Figures D.1c, D.1d, D.1e and D.1f). Moreover, the repeatability of the data collected with the first method considerably increases in this range of depth. Hardness in Inconel is an exception, as no plateau is reached, but the changing in hardness for larger contact depth than 550 nm is reasonably small (Figure D.1f). The comparison of elastic modulus measured with both methods is in very good agreement for both aluminium and Inconel (Figures D.1c and D.1d). This is a clear indication that there is a common background on the two methodologies. However, the comparison of the 2 methods in terms of hardness shows a slightly deviation in the case of Inconel, and considerable deviation in case of aluminium (Figures D.1e and D.1f). A discrepancy between hardness from quasistatic indentation and CSM has been repeatedly observed in elastoplastic materials. It can be remarkable especially in highly strain rate sensitive materials [15]. It will be discussed in Appendix E that both materials exhibit strain rate sensitivity to some extent. Incidentally, aluminium exhibits relatively high strain rate sensitivity and shows a larger deviation in hardness, while Inconel, which exhibits lower strain rate sensitivity, shows a much smaller deviation in hardness. This is in agreement with literature observations [15].

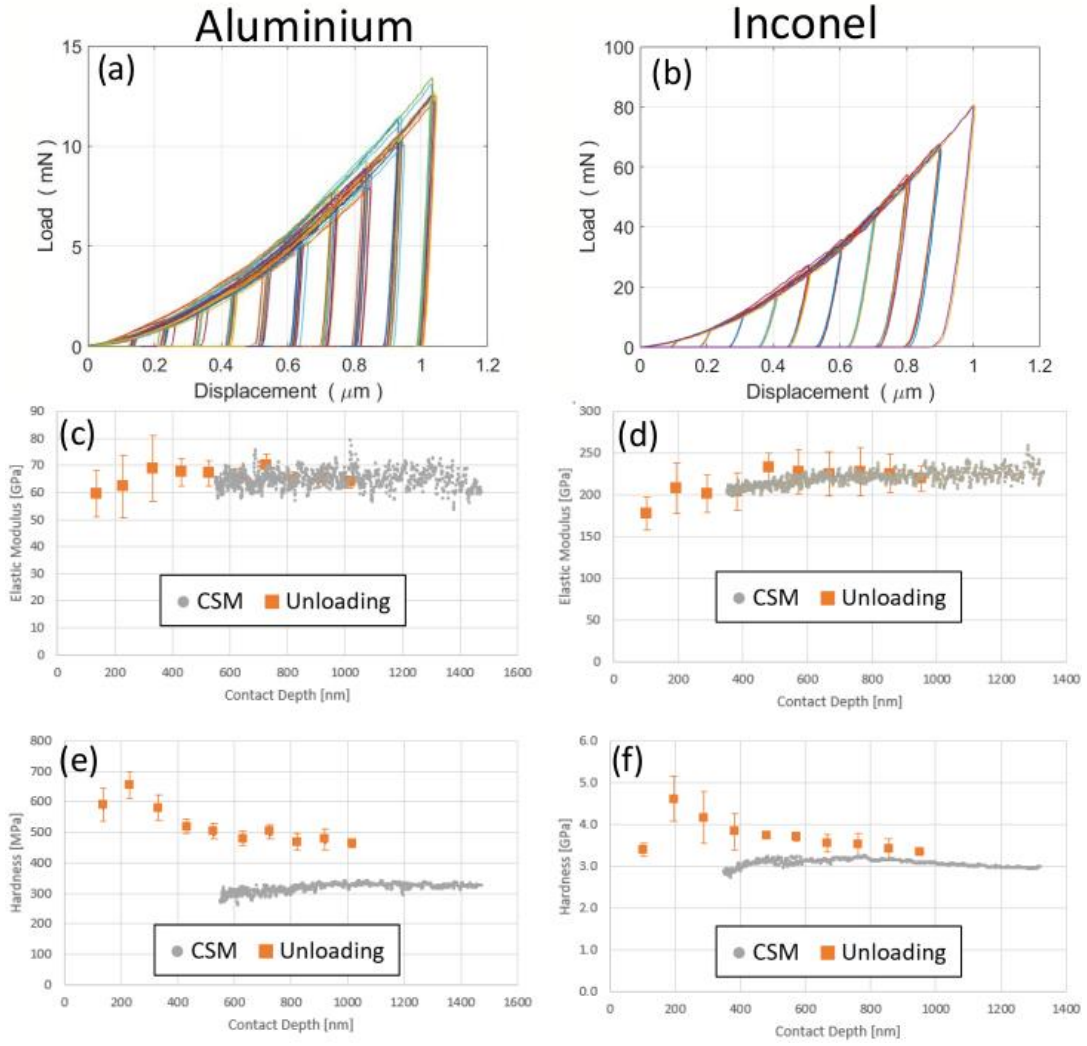


Figure D.1: Load-displacement curves from indentation having different maximum depth (in the range from 100 to 1000 nm) performed on (a) aluminium and (b) Inconel. (c) & (d) Elastic modulus, (e) & (f) hardness plotted as a function of the contact depth for both materials.

#### APPENDIX E (Strain rate sensitivity analysis on Al and Inconel with Berkovich indenter geometry)

Strain rate sensitivity coefficient ( $m$ ) upon indentation is defined as [38]:

$$m = \frac{\ln(H_2/H_1)}{\ln(\dot{\epsilon}_2/\dot{\epsilon}_1)} \quad \text{Eq. E.1}$$

where  $H_1$  and  $H_2$  are hardness measured at indentation strain rate  $\dot{\epsilon}_1$  and  $\dot{\epsilon}_2$ , respectively. The hardness must be measured at a sufficiently large depth to avoid any ISE.

The Indentation strain rate [39] in displacement control mode for a Berkovich indenter tip is calculated according to the following equation:

$$\dot{\epsilon} = \frac{\dot{h}}{h}$$

Eq. E.2

where  $h$  is the instantaneous depth and  $\dot{h}$  is the instantaneous displacement rate. Notice that, as  $h$  continuously increases during the loading stage of the test,  $\dot{h}$  must continuously increase in order to keep the strain rate constant. Conversely, in constant displacement rate indentation, as  $\dot{h}$  is constant, and  $h$  continuously increases during the loading stage of the test,  $\dot{\epsilon}$  must progressively decrease. In other words, constant displacement rate indentations are intrinsically not constant in strain rate. This is in contrast with what is observed in conventional mechanical testing such as tensile and compression tests, where there is a linear relationship between strain rate and displacement rate.

The most straightforward method to estimate  $m$  from indentation test is to perform several indentations with constant strain rate and measure the difference in hardness. However, this might not be convenient in practice, especially for relatively low indentation strain rates. Consider that a single indentation at  $10^{-4} \text{ s}^{-1}$  constant strain rate indentation test at 600 nm maximum depth lasts approximately 13 h. Even though it is technologically possible to perform such a very long indentation experiment, it is highly time consuming. Thus, alternate experimental protocols have been proposed in the literature.

The most common procedure to estimate  $m$  is based on strain rate jump indentation (SRJI) test [38]. Among the number of different protocols proposed on the literature, the one proposed in references [38] [40] has been selected in the present paper. The methodology consists in dividing the loading segment of a Berkovich indentation in 5 sub-segments organised as follows. Segments 1, 3 and 5 are named baseline segments and all of them have the same strain rate of  $10^{-2} \text{ s}^{-1}$ . Segments 2 and 4 are named jump segments and they have a strain rate of  $10^{-3} \text{ s}^{-1}$  and  $10^{-4} \text{ s}^{-1}$ , respectively. The loading segment is performed in CSM, in such a way to easily build a hardness vs contact depth plot, where the contact depth is also a function of the strain rate. It is important to perform the first jump test at a depth sufficiently large to avoid any ISE, in such a way that the hardness is depth independent. Equation E.1 can be readily applied to compare hardness from segments at different strain rates and extract the strain rate sensitivity. Each test has been repeated 3 times on both Inconel and aluminium. As fused silica is generally known to be strain rate independent upon nanoindentation in the selected strain rate range, it has not been tested for strain rate sensitivity. A CSM frequency of 10 Hz has been selected for both materials.

Figure E.1a and E.1b show the indentation curves of the SRJI test on Inconel and aluminium respectively. Curves were very repeatable, thus, only a single curve per material is shown for clarity. Notice that at the end of the loading stage there are 2 regions of the curve that clearly have different behaviours, which are the jump segments. Figure E.1c and E.1d show the elastic modulus, hardness and strain rate as function of contact depth. Elastic modulus is constant during the test in both materials, which is an indication that the selected parameters are optimal. Notice that the jump segments show a considerably larger scatter of the data compared to the baseline ones. This is because the strain rate is considerably smaller in jump segments, thus, at a constant sampling rate more points per nanometre are collected with a consequent increase of the scatter, this is in agreement with references [38] [40].

The estimated strain rate sensitivity coefficients are 0.00396 for Inconel and 0.0195 for aluminium. Thus, Inconel exhibits limited strain rate sensitivity while aluminium has a relatively high strain rate sensitivity.

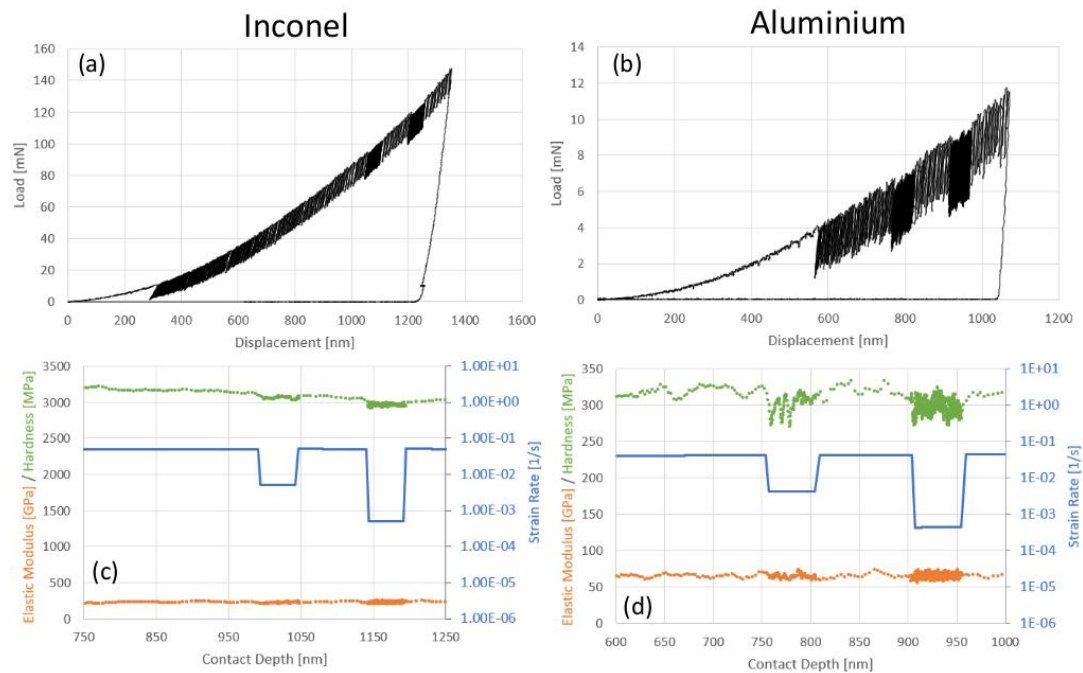


Figure E.1: Typical load-displacement curves from strain rate jump indentation test on (a) aluminium and (b) Inconel. Elastic modulus, hardness and strain rate as a function of contact depth for (c) aluminium and (d) Inconel.

## References

- [1] French Décret no 2012-1248 of 9th November 2012.
- [2] Maquet, P., Walker, C. I., Barnsley, R., Bertalot, L., Encheva, A., Pitcher, C. S., ... & Okayama, K. (2013). Development of ITER diagnostic window assemblies. *Fusion Engineering and Design*, 88(9-10), 2641-2645..
- [3] Aucott, L., Bamber, R., Lunev, A., Darby, T., Maquet, P., Gimbert, N., ... & Conway, B. (2020). Solid-State Diffusion Bonding of Glass-Metal for the International Thermonuclear Experimental Reactor (ITER) Diagnostic Windows. In *TMS 2020 149th Annual Meeti*.
- [4] Basu, S., Moseson, A., & Barsoum, M. W. (2006). On the determination of spherical nanoindentation stress–strain curves. *Journal of materials research*, 21(10), 2628-2637..
- [5] Bushby, A. J., & Jennett, N. M. (2000). Determining the Area Function of Spherical Indenters for Nanoindentation. *MRS Online Proceedings Library (OPL)*, 649..
- [6] Bushby, A. J. (2001). Nano-indentation using spherical indenters. *Nondestructive testing and evaluation*, 17(4-5), 213-234..

- [7] Collin, J. M., Parenteau, T., Mauvoisin, G., & Pilvin, P. (2009). Material parameters identification using experimental continuous spherical indentation for cyclic hardening. *Computational Materials Science*, 46(2), 333-338..
- [8] Herbert, E. G., Pharr, G. M., Oliver, W. C., Lucas, B. N., & Hay, J. L. (2001). On the measurement of stress–strain curves by spherical indentation. *Thin solid films*, 398, 331-335..
- [9] Pathak, S., & Kalidindi, S. R. (2015). Spherical nanoindentation stress–strain curves. *Materials science and engineering: R: Reports*, 91, 1-36..
- [10] Cackett, A. J., Lim, J. J., Klupś, P., Bushby, A. J., & Hardie, C. D. (2018). Using spherical indentation to measure the strength of copper-chromium-zirconium. *Journal of Nuclear Materials*, 511, 610-616..
- [11] Haušild, P., Materna, A., & Nohava, J. (2012). On the identification of stress–strain relation by instrumented indentation with spherical indenter. *Materials & Design*, 37, 373-378..
- [12] Jiri Nohava, Characterization of elastic-plastic (stress-strain) behavior of materials in small volumes by spherical indentation, Anton Paar Application Note, downloaded on Aug 2020..
- [13] Nohava, J., Hausild, P., Randall, N. X., & Favaro, G. (2010, November). Grid nanoindentation on multiphase materials for mapping the mechanical properties of complex microstructures. In *IMEKO 2012 TC3, TC5 and TC22 Conferences, Metrology in Modern Context*.
- [14] Randall, N. X., Vandamme, M., & Ulm, F. J. (2009). Nanoindentation analysis as a two-dimensional tool for mapping the mechanical properties of complex surfaces. *Journal of materials research*, 24(3), 679-690..
- [15] Leitner, A., Maier-Kiener, V., & Kiener, D. (2017). Dynamic nanoindentation testing: is there an influence on a material's hardness?. *Materials research letters*, 5(7), 486-493..
- [16] International Organization for Standardization. *Metallic Materials: Instrumented Indentation Test for Hardness*.
- [17] Tabor, D. (2000). *The hardness of metals*. Oxford university press..
- [18] Hay, J., Agee, P., & Herbert, E. (2010). Continuous stiffness measurement during instrumented indentation testing. *Experimental Techniques*, 34(3), 86-94..
- [19] Oliver, W. C., & Pharr, G. M. (1992). An improved technique for determining hardness and elastic modulus using load and displacement sensing indentation experiments. *Journal of materials research*, 7(6), 1564-1583..
- [20] Johnson, K. L., & Johnson, K. L. (1985). *Contact mechanics*. Cambridge university press..
- [21] Zhu, X. (2012, December). Tutorial on hertz contact stress. In *Opti* (Vol. 521, pp. 1-8). <https://wp.optics.arizona.edu/optomech/wp-content/uploads/sites/53/2016/10/OPTI-521-Tutorial-on-Hertz-contact-stress-Xiaoyin-Zhu.pdf>.
- [22] Hosford, W. F. (2006). The anisotropy of aluminum and aluminum alloys. *JoM*, 58(5), 70-74..

- [23] Liu, M. (2014). Crystal plasticity and experimental studies of nano-indentation of aluminium and copper..
- [24] Durst, K., Göken, M., & Pharr, G. M. (2008). Indentation size effect in spherical and pyramidal indentations. *Journal of Physics D: Applied Physics*, 41(7), 074005..
- [25] Swadener, J. G., George, E. P., & Pharr, G. M. (2002). The correlation of the indentation size effect measured with indenters of various shapes. *Journal of the Mechanics and Physics of Solids*, 50(4), 681-694..
- [26] Kermouche, G., Guillonneau, G., Michler, J., Teisseire, J., & Barthel, E. (2016). Perfectly plastic flow in silica glass. *Acta Materialia*, 114, 146-153..
- [27] Widmer, R. N., Groetsch, A., Kermouche, G., Diaz, A., Pillonel, G., Jain, M., ... & Michler, J. (2022). Temperature-dependent dynamic plasticity of micro-scale fused silica. *Materials & Design*, 110503..
- [28] Lacroix, R., Kermouche, G., Teisseire, J., & Barthel, E. (2012). Plastic deformation and residual stresses in amorphous silica pillars under uniaxial loading. *Acta Materialia*, 60(15), 5555-5566..
- [29] Topolski, K., Szulc, Z., & Garbacz, H. (2016). Microstructure and properties of the Ti6Al4V/Inconel 625 bimetal obtained by explosive joining. *Journal of Materials Engineering and Performance*, 25(8), 3231-3237..
- [30] Zeng, X., Liu, W., Xu, B., Shu, G., & Li, Q. (2018). Microstructure and mechanical properties of Al-SiC nanocomposites synthesized by surface-modified aluminium powder. *Metals*, 8(4), 253..
- [31] Ramachandramoorthy, R., Schwiedrzik, J., Petho, L., Guerra-Nunez, C., Frey, D., Breguet, J. M., & Michler, J. (2019). Dynamic plasticity and failure of microscale glass: Rate-dependent ductile-brittle-ductile transition. *Nano letters*, 19(4), 2350-2359..
- [32] Widmer, R. N., Bischof, D., Jurczyk, J., Michler, M., Schwiedrzik, J., & Michler, J. (2021). Smooth or not: Robust fused silica micro-components by femtosecond-laser-assisted etching. *Materials & Design*, 204, 109670..
- [33] Pero, R., Maizza, G., Montanari, R., & Ohmura, T. (2020). Nano-indentation properties of tungsten carbide-cobalt composites as a function of tungsten carbide crystal orientation. *Materials*, 13(9), 2137..
- [34] Zhang, G., Chandel, R. S., & Seow, H. P. (2001). Solid state diffusion bonding of Inconel 718. *Science and technology of welding and joining*, 6(4), 235-239..
- [35] López, B., Gutiérrez, I., & Urcola, J. J. (1992). Study of the microstructure obtained after diffusion bonding inconel 625 to low alloy steel by hot uniaxial pressing or hipping. *Materials characterization*, 28(1), 49-59..
- [36] Johnson, K. L. (1970). The correlation of indentation experiments. *Journal of the Mechanics and Physics of Solids*, 18(2), 115-126..

- [37] Phani, P. S., & Oliver, W. C. (2019). A critical assessment of the effect of indentation spacing on the measurement of hardness and modulus using instrumented indentation testing. *Materials & Design*, 164, 107563..
- [38] Maier, V., Durst, K., Mueller, J., Backes, B., Höppel, H. W., & Göken, M. (2011). Nanoindentation strain-rate jump tests for determining the local strain-rate sensitivity in nanocrystalline Ni and ultrafine-grained Al. *Journal of materials research*, 26(11).
- [39] Lucas, B. N., & Oliver, W. C. (1999). Indentation power-law creep of high-purity indium. *Metallurgical and materials Transactions A*, 30(3), 601-610..
- [40] Wehrs, J., Mohanty, G., Guillonneau, G., Taylor, A. A., Maeder, X., Frey, D., ... & Michler, J. (2015). Comparison of in situ micromechanical strain-rate sensitivity measurement techniques. *Jom*, 67(8), 1684-1693..